The Thesis Committee for John Thomas Lee
Certifies that this is the approved version of the following thesis:

Simulation and Experimental Investigation of Hot Forming of Aluminum Alloy AA5182 with Application toward Warm Forming

APPROVED BY
SUPERVISING COMMITTEE:

Supervisor:

Eric. M Taleff

David L. Bourell

Simulation and Experimental Investigation of Hot Forming of Aluminum Alloy AA5182 with Application toward Warm Forming

by

John Thomas Lee, B.S.

Thesis

Presented to the Faculty of the Graduate School of

The University of Texas at Austin

in Partial Fulfillment

of the Requirements

for the Degree of

Master of Science in Engineering

The University of Texas at Austin

May 2012

Acknowledgements

I would like to thank my advisor, Dr. Eric M. Taleff, for his insight and direction during the time spent on this study. I have gained a significant amount of technical knowledge through his teaching.

I would also like to thank Alexander Carpenter for helping me with many of the issues associated with setting up and running the experimental equipment and the simulation software.

Finally I would like to thank everyone else who helped with either technical or non-technical issues throughout my time in graduate school.

2012

Abstract

Simulation and Experimental Investigation of Hot Forming of Aluminum Alloy AA5182 with Application toward Warm Forming

John Thomas Lee, M.S.E.

The University of Texas at Austin, 2012

Supervisor: Eric M. Taleff

This study focuses on hot and warm forming properties of aluminum alloy AA5182 sheet, with attention toward warm forming, by using gas pressure to form sheet material. A temperature range of 300°C to 450°C and a pressure range of 690 kPa (100 psi) to 2410 kPa (350 psi) were used in a test matrix of twenty one different test conditions for gas-pressure forming of a sheet into hemispherical dome in a gas-pressure bulge test. Multiple sets of tensile data were used to develop a material model that predicts the dome height and shape of an axisymmetric bulge specimen at any given time during forming. In simulations of the forming process, 17 simulations of the total 21 experimental conditions showed good agreement with the experimentally measured dome heights throughout forming tests. The four cases that did not show good agreement

between simulation and experiment are a result of strain-hardening in the material during forming. Strain hardening was not significant in tension testing of specimens and was not accounted for in the material model, which considered only strain rates slower than for these experimental bulge testing. This demonstrates an effect which must be considered in future simulations to predict forming approaching warm conditions.

Two experimental bulge specimens were cross-sectioned post forming and grain sizes were measured to determine if grain growth occurred during the forming process. Experimental bulge specimens show no grain growth during the forming process. The tensile specimens from which the material model data were taken were measured to determine if plastic anisotropy was a possible issue. All specimens measured were proved to have deformed nearly isotropically. The results of this study show that predicting warm and hot forming of aluminum alloy AA5182 using gas pressure is possible, but that a more complex material model will be required for accurate predictions of warm forming. This is a very important step toward making hot and warm forming commercially viable mass production techniques.

Table of Contents

List of Tables

List of Figures

Chapter 1: Introduction

1.1 Overview

Warm forming is a very important concept for reducing the weight of vehicles for a variety of reasons. Making vehicles lighter has been part of the auto industry for decades. Aluminum was first used as a replacement in engine parts, but it is now also being looked at for other parts of the vehicle, particularly body closure panels [1]. Making a vehicle lighter increases fuel efficiency, lowers the power required needed for performance equal that of a heavier car, and improves emissions [1, 2]. In particular, aluminum and magnesium are two metals that are being used to help reduce the weight of vehicles. Aluminum and magnesium alloys can be quite strong but have low formability at room temperature. Thus, a new method of forming is required to form the complex parts needed in the auto industry [1]. Hot and warm forming are methods of increasing the formability of aluminum and magnesium, however warm forming of aluminum and magnesium is not currently very well understood, and thus has not been used in industry. Hot forming has been used in industry, but is typically done with certain alloys, such as SPF-grade AA5083, which, have particular properties amenable to hot forming [2].

Warm forming can be accomplished in a manner similar to superplastic forming (SPF) or quick plastic forming (QPF), where a sheet of material is clamped into a die and gas pressure is used to form the material into a die cavity [3,4,5]. In a paper on QPF, Taleff discusses the issues associated with defining a material model that can also predict thinning at certain areas of a die cavity. Taleff discusses QPF and its similarities to SPF,

albeit at faster strain rates and lower temperatures [3, 4, 5]. Warm forming follows a similar reduction of forming time and temperature from QPF, and can present similar problems [3].The idea behind warm forming is to determine temperatures lower than those of SPF or QPF but, at which there is still enough ductility in the material to form it into a relatively complex shape. Warm forming operations have the possibility to greatly reduce the cost associated with SPF or QPF through lower temperatures, less distortion of formed specimens during handling, and lower material costs. Many studies have been done on warm forming of aluminum; however, none of those studies have created a material constitutive model that enables accurate prediction of the forming process. In particular, although some prior models might enable accurate prediction of part thinning during forming, the prediction of forming time is still a significant challenge [6]. Using similar methods with a punch and die system at elevated temperatures there has been progress in determining the maximum force that is required to form a piece of aluminum into a die; progress has also been reported in the literature predicting the strain limits of forming those parts at elevated temperatures [6,7].

Forming parts using SPF or QPF has many benefits, including the ability to form complex part shapes while still using a single die, without the need for a stamp because the forming force is applied through gas pressure. However, some drawbacks to this method are that it can require a very high temperature and/or pressure to make sure that the material fully forms into the die. Another drawback to this system is that, depending on the temperature and pressure used, it can take a significant amount of time. Even

taking into account higher temperatures and pressures, these processes still take longer than a simple stamping process [8]. There is also an issue with how the material is processed before SPF, because the material must have a fine grain size, which can require expensive alloying and deformation processes prior to recrystallization [9].

The recent emergence of QPF in the auto industry has shown that it is a viable process to be used in the large scale manufacturing of complex part shapes [10]. Reducing vehicle weight by replacing heavier stamped steel parts with gas-pressure formed aluminum parts is one of the ways that the auto industry is looking to increase the fuel economy of vehicles. The present research is intended to support this pursuit of the industry. The purpose of this study is to conduct experimental and simulated gas-pressure bulge testing at hot and warm temperatures and to deliver a material constitutive model which can accurately predict forming times, dome heights and thickness profiles for a simple experimental geometry and forming process. The material that was chosen for this study is aluminum alloy AA5182, which has the composition shown in the table below, with other possible alloying elements in very small quantities (< 0.05 wt%), that in total do not exceed 0.15 wt. %. All values given are either a weight percent range, or a maximum allowed weight percentage [11].

Element	Al	Mg	Mn	Fe	Zn	Si	Cu	Cr	Ti
Weight %	Bal	4.0-5.0	0.2-0.5	.35	.25	.20	.15	.10	.10

Table 1-1: AA5182 Composition [11]

1.2 Background

1.2.1 Commercial Use of Gas Pressure Forming

There have been multiple studies on the fuel economy of automobiles and ways by which it can be improved. One of the more direct methods to increase fuel economy is to reduce vehicle weight. Because of added safety, performance and comfort features, average vehicle weight has increased over the past 20 years, highlighting the need to find new ways to incorporate lightweight materials into vehicles to increase fuel economy [12]. In recent years, automobiles have been manufactured with stamped steel body panels while other stamped steel parts, such as fenders or doors, are fastened on to the body [13]. If automotive steel sheet were simply replaced by aluminum sheet, the result could be a large decrease in vehicle weight, as seen in Table 1-2 [11].

Material	Carbon Steel	Aluminum Alloy 5182
Density	7.8g/cm^3	2.65g/cm^3

Table 1-2 Density of Carbon Steel vs. AA5182 [11]

However, due to the material cost and the low formability of aluminum at room temperature, the complex parts that are made with steel sheet cannot be economically replaced by aluminum [14]. The tensile ductility of AA5182 has been determined to increase by 2 to 3 times as temperature increases from room temperature to 300°C [3,15]. As can be seen in Figure 1-1, there is a large increase in elongation and a significant

lowering of the stress required to strain the material as the temperatre increases during uniaxial tensile tests.

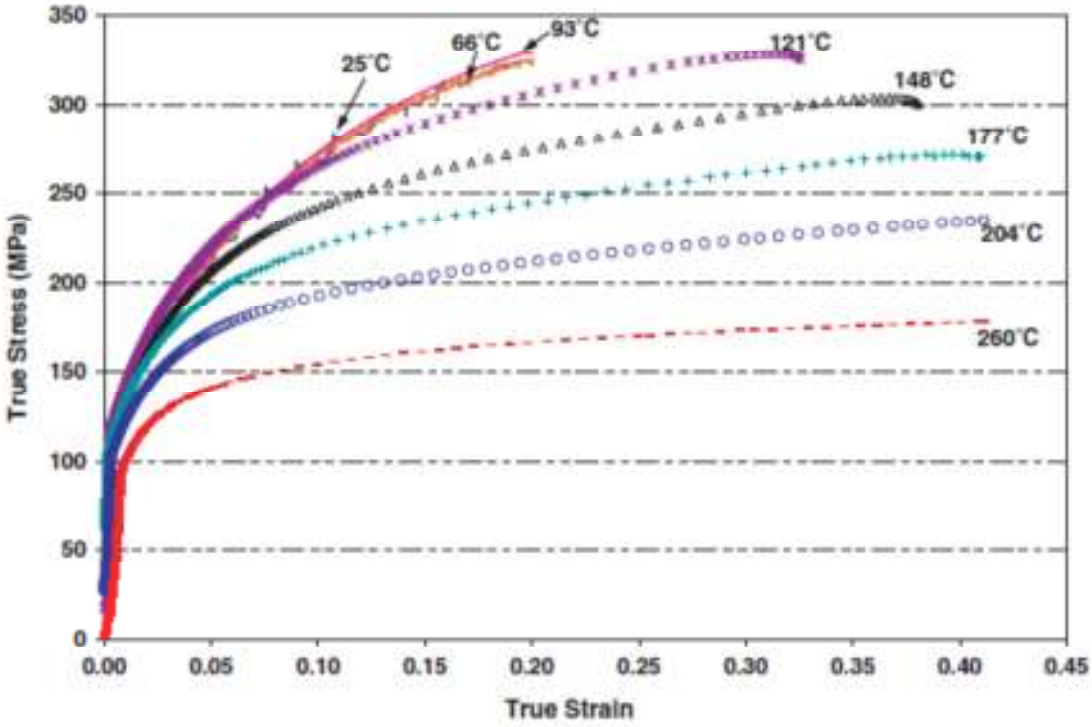

Figure 1-1 Uniaxial tensile test data for AA5182 from 25-250°C. [16]

Table 1-3 shows the properties for cold rolled steel sheet, 1000 series at room temperature. As can be seen in the last column, the elongation for all the types of steel except the high strength steel given are much higher than that of AA5182 at room temperature, shown in Figure 1-1[16].

Properties of Cold Rolled Steel Sheet				
Type	Yield Strength (MPa)	Tensile Strength (MPa)	Elongation in 50mm %	True Strain
Commercial	234	317	35	0.30
Drawing(rimmed)	207	310	45	0.37
Interstitial free	152	317	45	0.37
Medium strength	414	483	25	0.22
High strength	690	724	10	0.10

Table 1-3 The mechanical properties of cold rolled steel sheet, showing elongation of 1000 series steel at room temperature. [16]

Recent simulations have shown that gasoline consumption can be reduced by 0.3-0.7L/100km for every 100kg of weight reduction per vehicle [12, 17]. Weight reduction in the vehicle structure can also lead to reduction in certain performance requirements of other parts of the vehicle. For example, the same top speed or acceleration can be achieved with less horsepower for a lighter vehicle. Suspension components may be lighter if the vehicle body is lightened. These weight reductions in other parts of the vehicle are secondary weight reductions [17].

SPF has been commercially available since the early 1970s. Complex parts for vehicles have been made using SPF, and in the aerospace industry SPF has been used for almost 40 years [2,3]. Many of the components that have been created using SPF are structural components, meaning that they carry a load and must meet specific strength requirements. Examples include aircraft ejectors seats and fuselage fairings, as well as

electronic enclosures and undercarriage door panels [2]. Aluminum has been one of the top choices for SPF, and there are various aluminum alloys that have been used. Aluminum alloy AA5083 has long been the first choice for SPF because of its excellent ductility, over 300%, at elevated temperatures, its good service properties, and its reasonable cost [2]. Aluminum alloy AA5083 is very similar to aluminum alloy AA5182, which is a material investigated for use at the lower temperatures and higher strain rates required for warm forming. SPF requires a very fine grain size on the order of 10μm, very high temperatures, usually around 75% of the melting temperature, T_m, and very slow strain rates, on the order of 10^{-3} to 10^{-4} s^{-1} [3, 4]. AA5182 is not generally a viable material for superplastic forming because of its large grain size, which prevents deformation by grain-boundary sliding (GBS) creep, the primary deformation mechanism associated with a superplastic response [3, 18]. GBS requires a fine grain size and is the predominant deformation mechanism in SPF, where the temperature is much higher as well as the strain rate sensitivity [19]. Because of its alloy content, AA5182 generally cannot be processed for the fine, stable grain size typical of superplastic-grade AA5083 material [9]. However the coarse grain size of AA5182 does not exclude it from warm forming, where the main deformation mechanism is SD creep. SD creep is a dislocation creep mechanism that occurs in AA5182 at the temperatures used for warm forming, where the solute atoms are no longer barriers to dislocation motion but move along with dislocations creating a drag force against the dislocations [20].

1.2.2 Hot and Warm Forming

Hot forming of superplastic materials can give much greater tensile elongation and formability than possible at room temperature. Superplasticity, in a phenomenological sense, is the ability of an alloy to undergo extensive tensile deformation without necking prior to failure through rapid creep deformation [2]. One phenomenological equation for creep can be described using the Garafalo formulation, where Z is the Zener-Holloman parameter, A and B are material constants, n is the stress exponent, σ is the stress and E is Young's modulus. The strain-rate sensitivity and the stress are inversely related, m= 1/n.

$$Z = A*\mathrm{Sinh}(B\,\sigma/E)^{n} \tag{1-1}$$

The temperature dependence of the Zener-Holloman parameter can be seen in the equation below, where Q_c, is equal to the self-diffusion coefficient, R is the universal gas constant in Joules per mol*Kelvin , and T is the temperature in Kelvin.

$$Z = \dot{\varepsilon}*\, e^{Qc/RT} \tag{1-2}$$

AA5182 is a material that has poor tensile elongation at room temperatures, however increasing the temperature markedly improves the tensile elongation [21]. Solute-drag (SD) creep is the mechanism which gives AA5182 the additional elongation and formability at warm and hot temperatures [19]. Materials that exhibit GBS have a strain-rate sensitivity, m, between 0.5 and 1, while those that exhibit solute-drag creep have a strain-rate sensitivity of 0.25 to 0.33 [19]. Solute-drag creep is seen in AA5182

due to the addition of magnesium as an alloying element. Magnesium lowers the stress exponent, thus increasing the strain-rate sensitivity, compared to pure aluminum (m≈ 0.2) by inducing SD creep. This effect is shown in Figure 1-2 [19, 21].

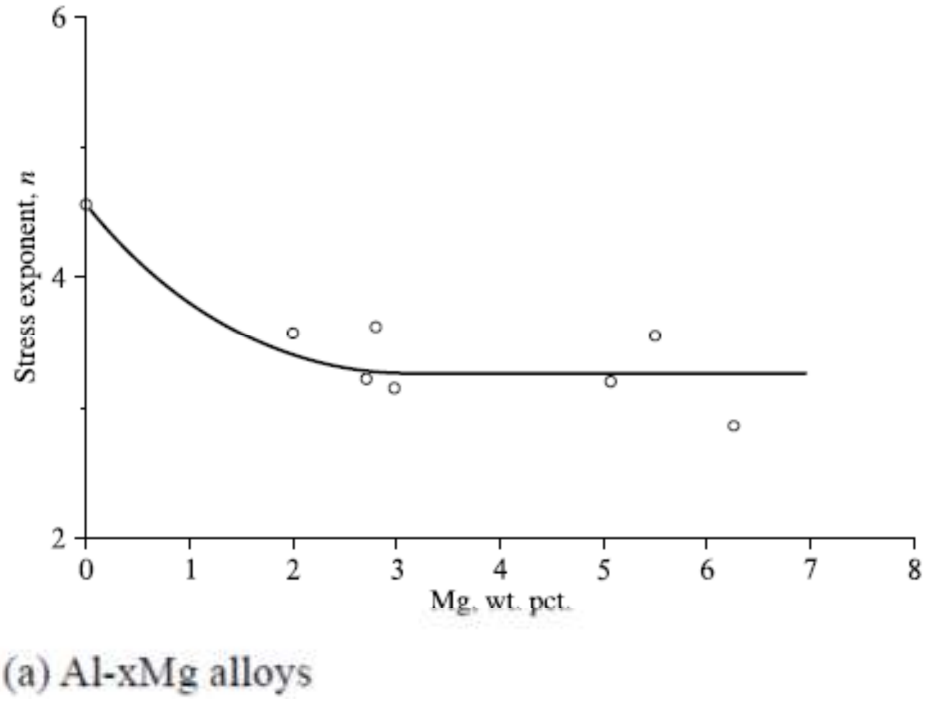

Figure 1-2 Stress exponent as Mg is added to an Al alloy. [19]

In a common dog-bone style tension test, a specimen is elongated along a single axis. Prior to rupture, the specimen may neck, a localized shrinking in cross sectional area. Superplastic materials are able to achieve greatly increased tensile deformation without necking, largely by having higher strain-rate sensitivity, m, than other such materials. A higher strain rate sensitivity, usually 0.2 for non-superplastic metals, but >=0.5 for superplastic materials, helps avoid necking during deformation.

A conventional material in a tensile test at room temperature will stretch in one direction while its cross-section becomes smaller. The material will experience work hardening, and the load will continue to increase until reaching the ultimate tensile strength. At this point, the work hardening rate of the material will be unable to prevent a local reduction in cross-sectional area, and the material will neck while the overall load will decreases until fracture. Strains local to the necked region may be quite large, but occur over a very small length (along the tensile axis). Thus, the elongation of the entire specimen is not necessarily large. In superplastic materials, localized necking is greatly reduced. During a tensile test of a superplastic material at elevated temperature, when localization starts, the strain rate becomes slightly higher in this region. Because stress and strain rate are strongly related, $\sigma \propto \dot{\varepsilon}^m$, the stress also increases, which prevents additional localized reduction in this region. What this means is that the strain is spread out over the entire specimen. This allows large elongations before the strain rate in a neck becomes significantly larger than the other regions. This process is directly related to the strain rate sensitivity, and the higher the strain rate sensitivity, the smaller the strain rate difference between the localized necking area and the other areas of the specimen, allowing a greater elongation. Thus a higher *m* value results in a larger possible elongation value [22]. Although a high strain-rate sensitivity is a necessary requirement for a superplastic response, it is not alone sufficient. A superplastic material must also avoid rupture during plastic deformation as a result of internal damage, such as cavity nucleation and growth.

Warm forming can be accomplished at much lower temperatures and faster strain rates than are used for superplastic forming. Warm-forming can take advantage of solute-drag creep to achieve good ductilities, and the material does not require a fine grain size [3]. Faster forming rates in warm forming can result in increased production rates in industry. Eliminating the requirement of a fine grain size can reduce material cost. Another improvement that could be overlooked when discussing the differences between superplastic forming and warm forming is the reduction in potential part distortion during handling when the lower temperatures of warm forming are used. Lower temperatures allow for much easier handling of parts that have already been formed, especially during part removal from the die. Warm forming may provide improvements in cost and time over SPF. Less expensive materials, faster production, lower temperatures, less part distortion, and easier material handling are the main advantages of warm forming over SPF. However, warm forming cannot achieve the degree of part complexity possible with SPF, and this can be an important limitation.

1.2.3 Die Forming

Currently warm forming is not a process that is used significantly in industry due to the lack of knowledge surrounding the complexities of the forming process. Commercial superplastic forming is typically accomplished by clamping a sheet of metal between two die halves while gas in blown in from one end to form the material into the die half on the other side. Difficulties with predicting the forming rate of the material include, but are not limited to, friction between the material and the die, the shape of the

die including the die entry radius and the angle of the die [23]. There are four separate regions considered when dealing with bulge forming into a closed die. Those four regions are: free bulge region, die contact entry region, sidewall contact region and bottom contact entry region, as shown in Figure 1-3 [23].

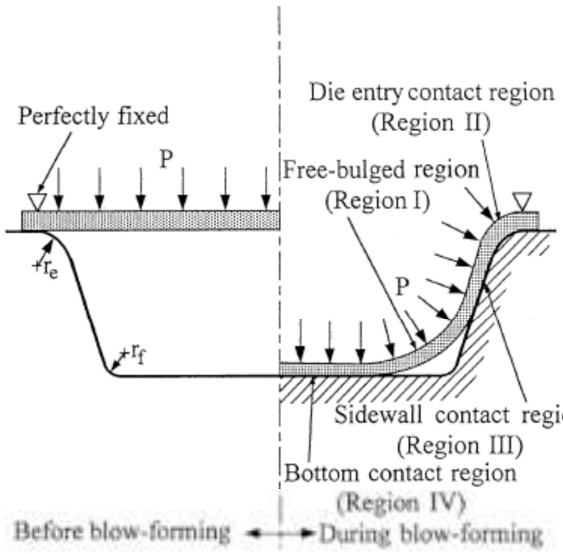

Fig. 2. Schematic illustration of the contact relationships between the sheet and die during blow-forming process.

Figure 1-3 Depiction of gas pressure forming of a sheet of material in to a die. [23]

Only two of the four regions in a closed die scenario are applicable to the forming tests of this research study. The die contact entry region, where the material is touching the entry radius of the die, will be present in all cases of gas-pressure forming. The free bulge will also be present in all cases of gas-pressure forming, for at least some period of time. For forming into a closed die, the free bulge region slowly disappears and the sidewall and bottom contact regions become a larger portion of the total sheet surface area. The free bulge region ends once contact is made with the wall or bottom, and the

forming, in most cases, will be finished once there is no remaining free bulge region, but complete contact with the die. These four regions can also be broken down into three total phases. The first phase is when only the first and second regions apply, which is the free bulge region. The second phase is when contact with the die is first made at either the bottom of the die or along the sidewall. The final phase is determined as when the remaining region, whether it is the side contact or bottom of the die, is contacted by the sheet. At the end of phase three, the die forming process has been completed, and there is no remaining free bulge region [23]. When the sheet is in contact with the sidewall or bottom of a die, frictional forces act upon the material, making numerical predictions of forming much more challenging. Data taken from Hwang et al. [23] in Figure 1-4 shows that the effect of the coefficient of friction can significantly change the forming time.

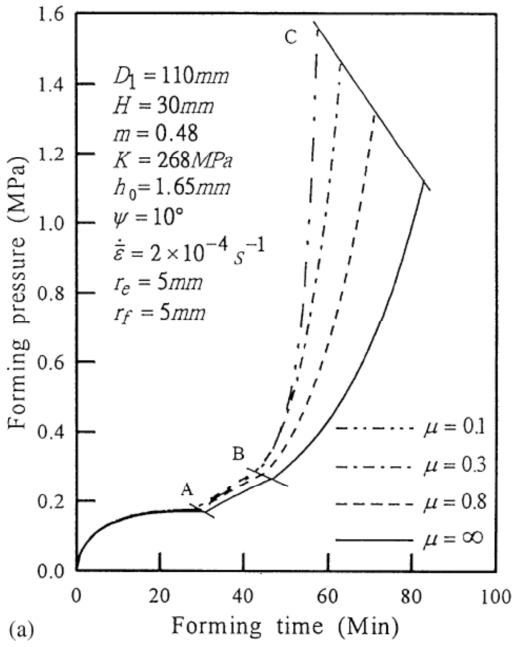

Figure 1-4 Forming times as a function of coefficient of friction of AA5182, [23]

This experimental study uses an open die, not a closed die, and will only be concerned with the first phase of forming. These experiments produce an axisymmetric bulge dome that will only experience die contact entry and free bulging. This reduces many of the complexities that are associated with predicting forming. Some of the extra complexities involved with forming a sheet of metal into a closed die are not intrinsic material properties, but are properties that are dependent on the die itself, its interaction with the sheet, and also any lubricant that is used between the die cavity and the material to be formed. The forming experiments of this investigation will be focused solely on the intrinsic material properties of aluminum alloy AA5182, and thus an open die free bulge test was chosen to minimize other factors.

1.3 Material Properties

AA5182 contains magnesium as the primary alloying element, which is added for strengthening, and increases ductility at elevated temperatures due to the benefit of solute drag creep [21]. As shown in Figure 1-5, at warm temperatures, elongation is increased as more magnesium is added to aluminum. AA5182 contains 4 to 5 weight percent magnesium, and thus would fall between the Al-3%Mg and Al-6%Mg lines in Figure 1-5 [24]. AA5182 is a generally a coarse grained alloy, with grain sizes of roughly 15 μm, which make it unsuitable for SPF. But, SD creep makes it is a very good candidate for hot and warm forming operations [19].

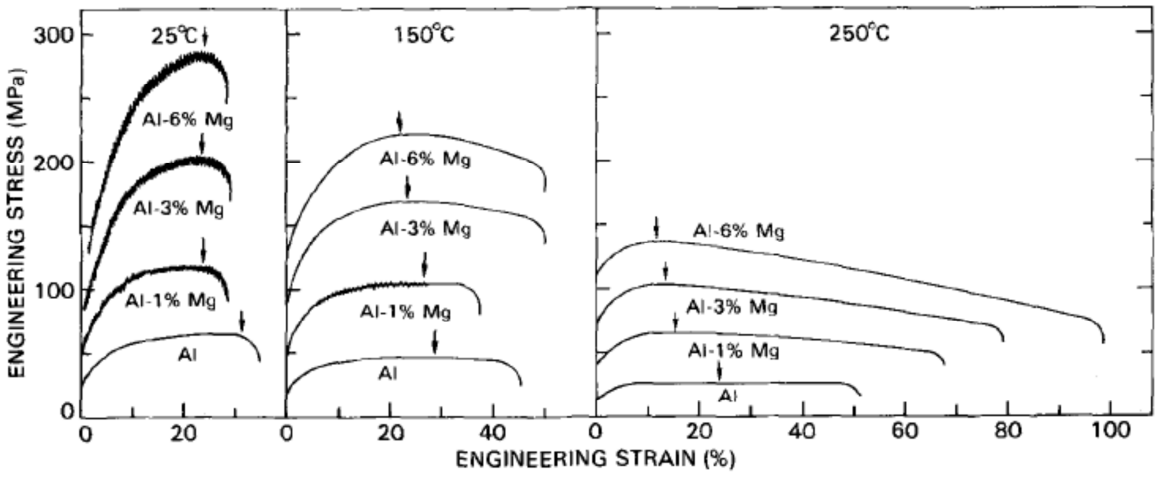

Figure 1-5 Effect of adding Magnesium on Aluminum at varying temperatures, [21]

Multiple studies have been done on AA5182 and its tensile properties at elevated temperatures. The Young's modulus of AA5182 varies with temperature, which can be approximated as that of a pure Al using the data from Köster [25] using Equation 1-3 [9].

$$E = 77{,}630 - 12.98\,T - 0.03084\,T^2 \qquad (1\text{-}3)$$

Where E is in GPa, or newtons per meter * 10^9, and *T* is in Kelvin. Knowing how Young's modulus changes with temperature is an important piece of information when dealing with a material over a large range of temperatures. Over the range of temperatures studied in this investigation, the Young's modulus varies by almost 15 GPa. This is a significant change in the modulus over a range of 150°C.

Figure 1-6 shows experimental data from tensile tests of AA5182 from Brian Chang [9].

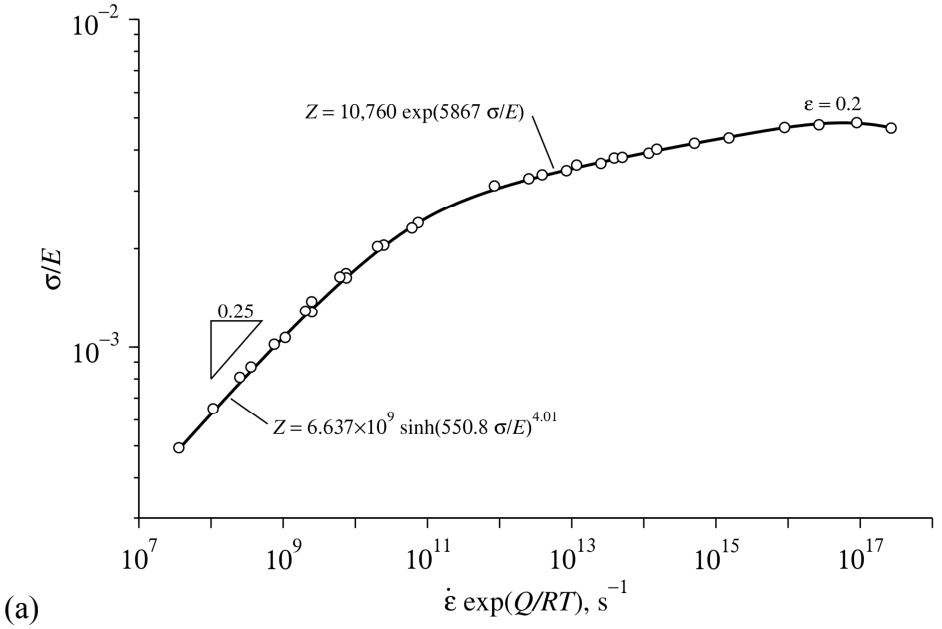

(a)

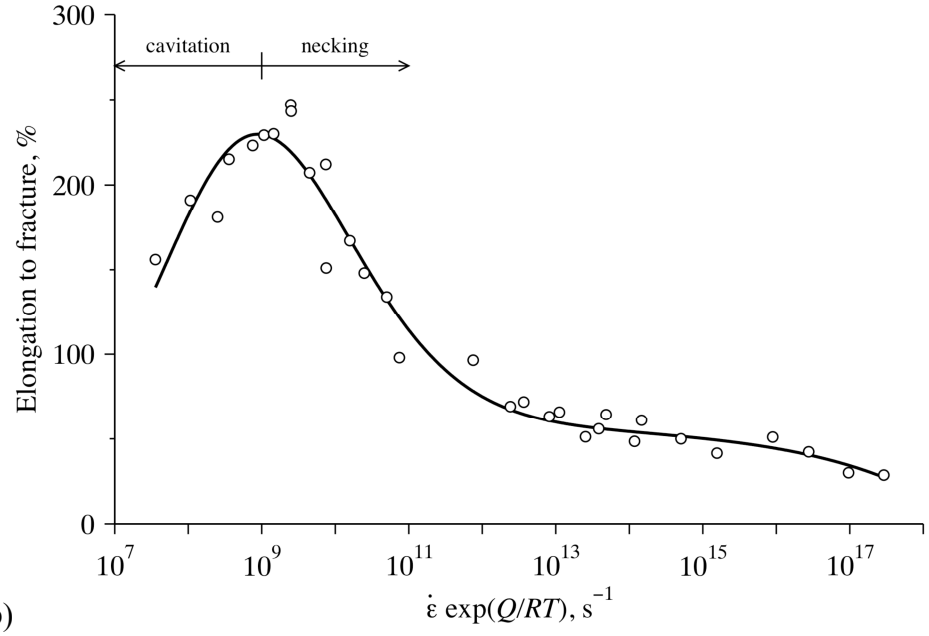

(b)

Figure 1-6. Tensile-test data are shown for 1-mm AA5182 sheet as a function of Zener Holloman Parameter for (a) σ/ε, (b) elongation to fracture. [9]

In Figure 1-6(a), it is shown that Chang et al. [9] was able to fit an equation for Z as a function of σ/ε to these data using a hyperbolic sine function at low values of *Z* [9]. He used two different exponential functions at high values of *Z*. The break in these two regions shows that the material undergoes a change of deformation mechanism which is dependent on the value of *Z* [3]. These graphs also show the variation in ductility of AA5182 with *Z*. It was determined that the AA5182 material would be very useful for warm forming, due to the high ductilities observed at warm forming temperatures, and will most likely fail through thinning or necking of the material [3]. AA5182 shows enough ductility at moderate *Z* values to be a useful alloy for warm forming conditions.

1.4 Solute Drag Creep

Magnesium forms a substitutional solid solution in aluminum, which elastically distorts the crystal structure, due to differences in atom size between aluminum and magnesium, and impedes movement of dislocations, which in turn gives the alloy additional strength. Substitutional solid solution strengthening is also not particularly temperature dependent, which gives it an advantage over other methods of strengthening [1]. This effect can be manifested as SD creep at elevated temperatures. SD creep is a type of dislocation creep mechanism that can occur at high temperatures. As with other dislocation creep mechanisms, it is rate dependent on the thermally activated process of diffusion. At elevated temperatures, the solute atoms no longer act as static barriers to dislocation motion but form a mobile atmosphere around them, creating a drag force on dislocations [20]. This solute-drag process is the characteristic rate-controlling process of

SD creep. It can be differentiated from other creep mechanisms by strain-rate sensitivity (m = .25 to .33), activation energy (equal to that for solute diffusion) and the primary creep stage (SD creep exhibits an inverted primary) [1, 26, 27]. The strain rate follows the equation:

$$\dot{\varepsilon} = A \exp(-Q_c/RT) (\sigma/E)^n \quad (1\text{-}4)$$

The stress exponent $n = 1/m$, E is the dynamic unrelaxed elastic modulus, Q_c is the activation energy for creep, and A is a material constant. Alloys that have $n = 5$ and Q_c equal to the activation energy for lattice self-diffusion are known as Class II alloys, for which creep rate is controlled by dislocation climb, as in most pure metals. Those that have $n = 3$ and Q_c equal to the activation energy for solute diffusion are known as Class I alloy, in which creep is controlled by a viscous glide mechanism. This process slows dislocations during glide to such an extent that the glide step is much slower than climb [26]. Viscous glide and dislocation climb are two sequential processes and, thus, are dominated by the slower of the two processes in the overall deformation rate. Change between a Class I and Class II alloy behaviors can be accomplished by increasing the solute content in the alloy [26, 27]. During solute drag creep the solute atmosphere is moving during deformation by way of diffusion of the solute atoms. When a dislocation moves, it must push its way through the solute atmosphere, slowing the velocity with which the dislocation can move. [20]. The overall velocity of the dislocation, $v_{dis,}$ then is a result of Equation 1-5 where M is the dislocation Mobility and F is the force applied to the dislocation by the solute atoms [28].

$$v_{dis}=MF \quad (1\text{-}5)$$

Solute drag creep can be viewed as a competition between the rate of formation of a solute cluster around a dislocation and the velocity of that dislocation. The dislocation is trapped by the solutes, which will diffuse towards the dislocation, until the dislocation is able to move on through thermal activation. This process is repeated again, which slows down the deformation of the material [29].

1.5 Problem Statement

This main focus of this study is to look at hot and warm forming of aluminum alloy AA5182. The results of this study include determining the possible conditions for forming, creating a material constitutive model to describe the behavior of the material over those possible conditions, and determining at which specific conditions this model can describe the behavior of the material to a satisfactory degree. The material constitutive model should be able to accurately describe the forming time to a specific dome height with a reasonable certainty, as well as accurately describe the shape of the bulge specimen at the final dome height.

Chapter 2: Experimental Procedures and Simulation Methods

2.1 Experimental Equipment

The experimental tests were conducted using a servo-hydraulic testing machine and a bulge testing device designed by Ricardo Vanegas, as shown in Figure 2-1 [30].

Figure 2-1 UT Bulge Testing Machine

The system is designed to connect to a servo-hydraulic uniaxial testing machine and uses a clamshell style furnace for heating the dies and test specimens. To achieve the required pressure for bulge forming, a portable gas cylinder is used, as shown in Figure 2-2, which is connected through piping to the top die.

Figure 2-2 Portable cylinder attached to regulator and two way valve

There is a regulator attached directly to the portable gas cylinder, which controls the amount of gas pressure that is delivered to the specimen during testing. For the experiments that were run, commercial grade nitrogen was used as the gas for forming

the test specimens. The die consists of two vertical tubes; the top tube is part of the gas delivery system. The bottom tube serves as the open half of the die, and houses a linear measurement system that is used to track the specimen's dome height during testing. There are two valves attached to the gas delivery system to control when and where the gas flows. The first is a simple two way valve attached to the pressure regulator to control the gas to the rest of the system. There is a second three-way valve which can a) be closed, b) deliver the gas to the top tube assembly, or c) vent the gas from the top tube assembly. After this second valve, the piping leads directly in to the top tube assembly, which delivers the gas pressure directly to the test specimen.

Figure 2-3 shows a schematic cross section of the entire die fixture, gas delivery system and clamshell furnace system. This figure was taken from the thesis of Ricardo Vanegas [30], and shows the end of the gas delivery system going through the top tube, as well as the two parts clamped together forming the die. The linear measurement system is shown in the lower die, running down the length of the entire bottom column. The gas delivery system runs from the portable cylinder through multiple valves and corners in the metal piping.

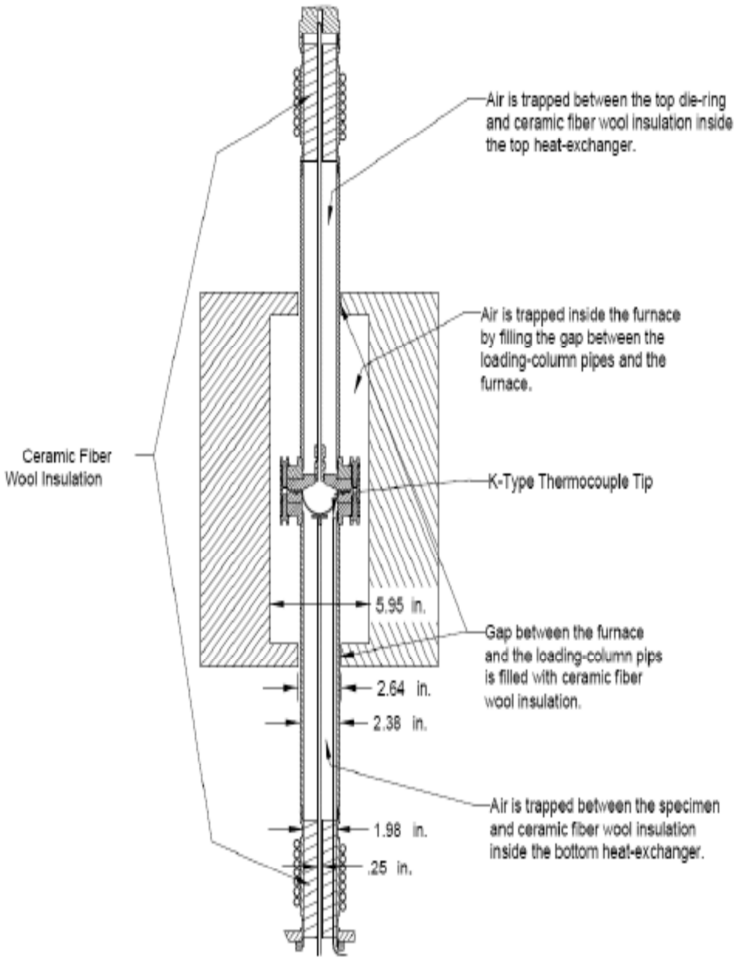

Figure 2-3 Schematic of column rods and clamshell oven, taken from thesis of Ricardo Vanegas [30]

A study was conducted to determine if there was any pressure loss in the system. A second pressure regulator was attached at the end of the piping, at the top of the top column in Figure 2-3. The first regulator was set to the values to be used during experimental testing, and the readings from the second regulator were used to determine the overall pressure loss. A large pressure loss would require a higher pressure at the gas cylinder regulator to achieve the pressures desired at the forming die end. The results

from the pressure loss testing are shown in Table 2-1. The difference in the pressure values can be attributed to some loss, as well as some variation in the accuracies of the two pressure regulators used. The pressure difference is not significant enough to cause any concern for testing.

Regulator Pressure, kPa (psi)	Pressure Gage Measurement, kPa (psi)
690 (100)	680 (98)
1030 (150)	1010 (147)
1380 (200)	1350 (196)
1720 (250)	1700 (247)
2070 (300)	2040 (296)
2410 (350)	2400 (348)

Table 2-1 Results from pressure loss testing of gas delivery system

The test specimen is a flat disk of roughly 96 mm (3.8 inches) in diameter by 1mm thick. This test specimen is placed in the bottom die and clamped by die force applied through the servo-hydraulic frame. An air-tight draw bead, shown in Figure 2-4, is created between the two dies to keep the gas from leaking. The outer diameter of the draw bead is roughly 76 mm in diameter, and the inner diameter is 64 mm in diameter.

This draw bead creates the seal that allows the gas pressure to form the material. The draw bead also holds the specimen in place, so that it does not move during the testing.

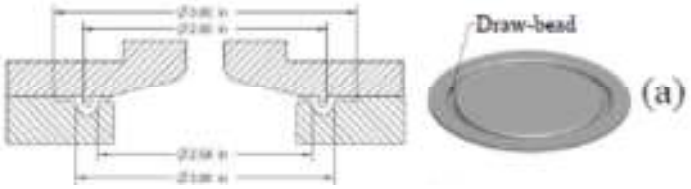

Figure 2-4 Schematic of clamped columns rods showing draw bead, taken from thesis of Ricardo Vanegas [30]

As shown in the schematic in Figure 2-3, there is a linear measurement system that tracks the dome height of the test specimen during the experimental bulge test. This linear measurement system, designed and constructed by Ricardo Vanegas [30], involves a measuring rod inside of the bottom column which is attached to a low friction pulley system and a micrometer. The top of the linear measurement system is shown, along with the draw bead in the bottom column, in Figure 2-5.

Figure 2-5 Measuring rod inside bottom column

The top of the linear measurement rod shown in Figure 2-5 is gently pressed against the bottom of the test specimen before testing as the specimen bulges downward into the lower column, this rod is pushed downward and moves a micrometer positioned in the lower portion of the linear measurement system, as shown in Figure 2-6.

Figure 2-6 Linear Measurement System. A) Micrometer B) Measurement Rod C) Measurement Beam

The linear measurement system uses a micrometer, measurement rod and the measurement beam. The measurement rod pushes down on the measurement beam, which moves the micrometer spindle down to record the dome height change. This system was designed to be low friction to allow for the dome to bulge downwards without any resistance from the measurement rod. The micrometer is connected to a

laptop computer, through which the dome height is logged in to a Microsoft Excel file for later analysis.

A total of two samples were mounted, ground and polished and then etched using an electrolytic process with Barker's Reagent (5ml of HBF_4 in 100ml of H_2O) at a voltage of 25 volts. Optical photomicrographs were then taken digitally of each specimen for comparison using polarizing filters to clearly see the different grains.

2.2 Simulation Methods

2.2.1 ABAQUS Background

ABAQUS™ [31] is a finite element modeling program that is used here for simulating the gas pressure forming of the aluminum. ABAQUS™ requires two separate files, one that characterizes the material and a second that characterizes the test that will be run. The material file, or material model, was created using elevated temperature tensile data taken from the data of Brian Chang [9]. This resulted in a constitutive model that can be used to describe the way the material will react when it is placed under the conditions described in the test file. The bulge test file was adapted from a similar test file developed by Alex Carpenter [32]. The bulge test file was modified to ensure that it would work with the new material model that was created. The simulation figures are taken from ABAQUS viewer, which gives a graphical view of the deformation process.

2.2.2 Bulge Test

The bulge test file controls the pressure of the test and is a two-dimensional, axi-symmetric wire frame model of both the blank and a die. The blank and die are two separate sets of points that are described in the file on an x-y grid. The size of the blank model that will be used for the experimental testing is 51 mm in diameter, or roughly two inches. The FEM model is an axisymmetric two dimensional wire frame of the circular specimen and die, which can be extruded about 360° to give a three-dimensional rendering of the material. This is done after the simulation has been completed to give a clearer view of the now deformed material. Figure 2-7 shows the wire mesh model, swept around 180° to give a cross sectional view of a 3-D rendering of the specimen and die.

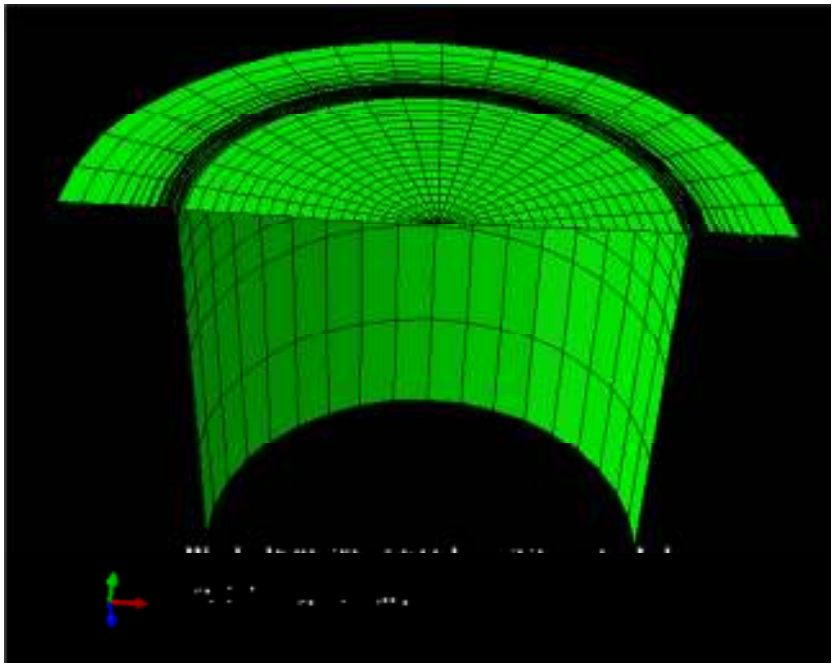

Figure 2-7 3-D rendering of a 2-D wire frame model, created by sweeping 180° around the center point

The two-dimensional model used in these simulations is based on the work of Paul Sherek, who proved in his thesis that predictions from the two-dimensional ABAQUS model did not differ from those of a three-dimensional model [33]. The simpler two-dimensional model is used to reduce the time of the simulations as well as avoid the difficulties that may occur with a more complex bulge file.

The bulge test file defines a two-step process, an elastic step for one second, which bulges the material using elastic deformation to get started, followed by a plastic deformation process, which is described in the material model file. This elastic step is used to create a small bulge in the material before moving on to the testing stage and is an important part of getting the simulation to run. This is an important step because the test files use the equation for pressure in a thin-walled pressure vessel.

$$\sigma=(p*r)/(2*t) \tag{2-1}$$

In this equation stress, σ, is equal to the pressure, p, multiplied by the radius of curvature of the specimen, r, divided by two times the thickness, t. If the plate were to start flat, the equation would yield an infinite stress because the radius of curvature of a flat plate is infinite. The initial elastic step deals with this issue by deforming the material initially to create a non-infinite radius of curvature.

In a select few of the simulations, the static step was not enough, and a small initial curvature was added to the blank model for these cases. Across the radius of the die, the material was given a height increase of 0.6 mm at the very center node decreasing to 0.0

mm at the edge node. The model shows what would be positive dome height in the downward, or negative y, direction, to mimic the experimental set up that is used. The 0.6mm increase in height is large enough to avoid the infinite stress problem, but is also small enough that the overall validity of the simulation is not compromised. This issue is also addressed after the simulations have been run during the data analysis of the results.

The die for the material is created similarly to the material, forming the edge of the die as well as the die wall. The nodes for the blank model that are outside of the test area are programmed to stay stationary throughout the test. In an experimental test this area of the specimen will be clamped between the bottom half of the die and the top half, which is also the gas delivery system, thus holding them in place.

2.2.3 Bulge Test Verification

The FEM input file that is used in the simulations was adapted from a previous input file created by Alex Carpenter; the new file must be verified to work correctly [32]. To verify that the resulting simulation does correctly apply the gas pressure to a specimen and does not have any errors, it was compared against the results from Carpenter [32]. As shown in Figure 2-8, using the same material model and running two bulge simulations at 450°C and 150 psi, the two simulations produce nearly the same dome height vs. time plot.

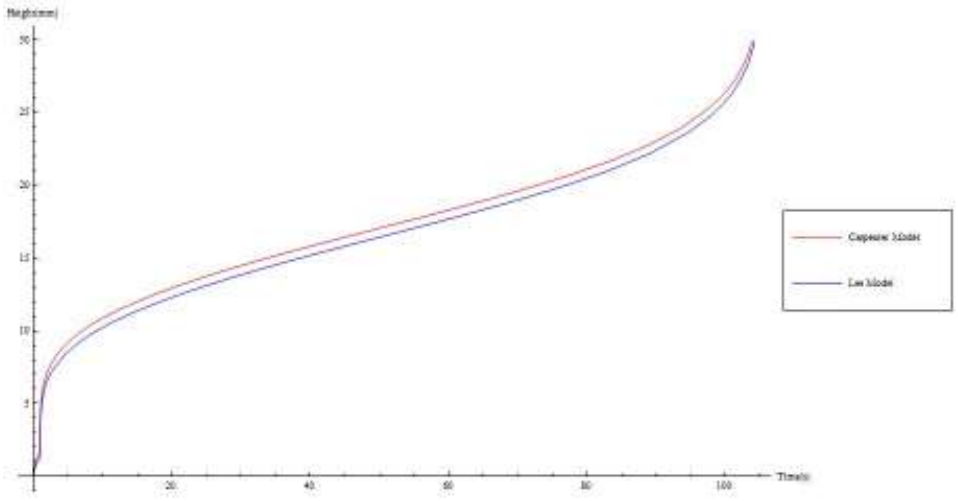

Figure 2-8 Lee bulge simulation compared against Carpenter bulge simulation using the same material model at a temperature of 450°C and a pressure of 150 psi

The plot shows the original Carpenter model in red, while the blue line shows the updated model. Achieving the same dome height result over a test to a 30mm dome height verifies that the bulge simulation is correctly predicting the physics required to bulge a specimen using a set temperature and pressure. These bulge simulations were conducted using a previous material model, verified by Carpenter [32].

As well as verifying the bulge simulation, it is important to determine that the mesh being used to define the material is sufficient for testing. Verifying that a) the mesh had converged and b) using a finer mesh would not change the results of testing, three separate meshes were created and tested using the same conditions and the same material model. The standard mesh that was originally being used had 41 elements defining the

material over a distance of 32.4 units. The material that was being deformed had nodes placed 1.5 units apart, with the mesh getting finer as it approached the corner of the die. The two extra meshes that were used to determine convergence used twice as many points spaced at half the distance and 4 times as many points spaced at a quarter of the distance of the original mesh. The mesh sensitivity study was conducted at a pressure of 250 psi and 400°C. In Figure 2-9, the original mesh is blue dots while the finest mesh is shown as red diamonds. The two results are overlaid at a constant time of 47 seconds, showing that there is no difference in either the shape or the total deformation of the specimen.

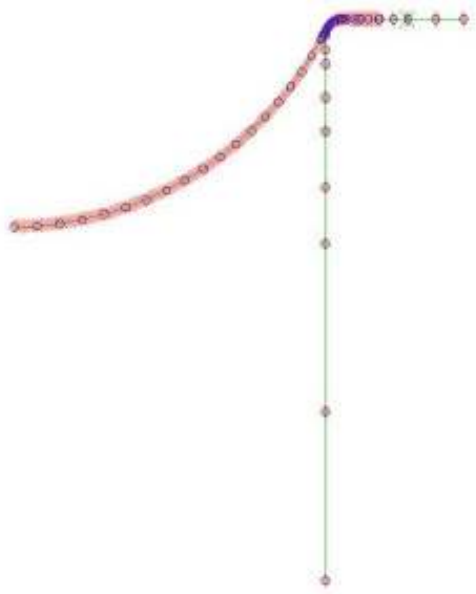

Figure 2-9 Overlay of finest mesh(red) over standard mesh(blue) bulge file during deformation

As shown in Figure 2-10, both simulations exhibit the same deformation throughout the entire test. While there is a slight divergence at the very end of the test

between the two meshes, at that point in the test the specimen would have become too thin and failed, so the difference is not relevant.

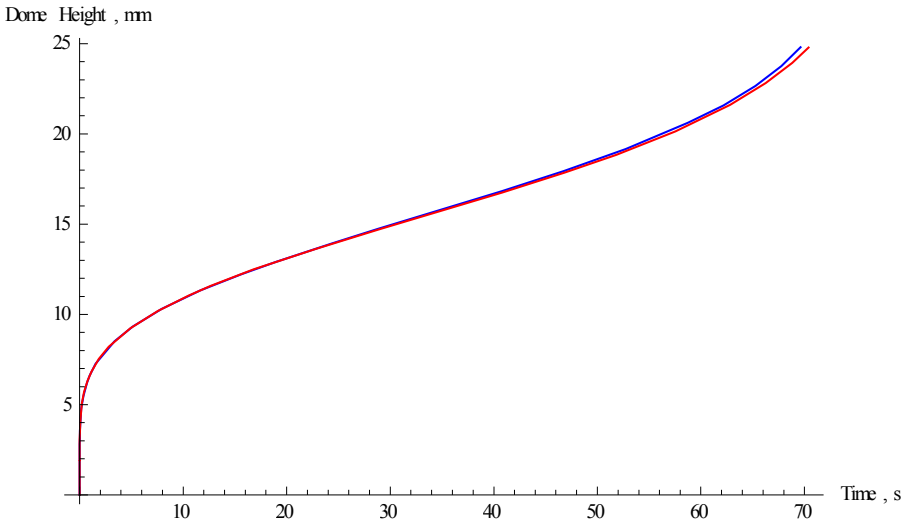

Figure 2-10 Graph of dome heights vs. time comparison of regular mesh(blue) and finest mesh(red) simulation bulge test

The bulge test file has been completed and verified to work correctly, while both the element type and the mesh being used are appropriate for the testing conditions.

Chapter 3: Material Model and Verification

3.1 Material Constitutive Model

A large amount of work has been done to predict the bulge and tensile testing of aluminum and magnesium alloys at hot temperatures, and to a lesser extent warm temperatures [10, 18, 19, 21]. Multiple equations have been developed to determine the behavior of aluminum at warm temperatures [9]. The overall material model is made up of the three following separate equations, of which the first two have already been mentioned. The first model predicts elastic response, using;

$$E = 77630 - 12.98T - 0.03084T^2 \tag{3-1}$$

Equation 3-1 describes the Young's Modulus of the AA5182 material at a specific temperature, where E is the Young's Modulus and T is temperature in Kelvin. [9]. Testing is done at a constant temperature and thus the overall Young's Modulus value is constant for each individual test, but varies amongst the scope of all tests. As temperature increases the Young's Modulus decreases. The second model predicts plastic response, as;

$$Z = \dot{\varepsilon} * e^{Qc/RT} \tag{3-2}$$

Equation 3-2 is the Zener-Hollomon equation, which relates the activation energy of creep in the material (Q_c), the universal gas constant (R), the temperature in Kelvin (T) and the plastic strain rate of the material to the Zener-Hollomon parameter, Z. The

Zener-Hollomon parameter is used because of the ability to compare multiple tests across different strain rates and temperatures. The ability to compare simulations across multiple strain rates, or pressures, and temperatures is vital in developing a material model that accurately predicts the testing across all of the test conditions.

The third equation used in the material model, Equation 3-3, is of the Garofalo formulation, which relates the Zener-Hollomon parameter to stress (σ), Young's Modulus (E), and the stress component, n. These are related through two constants A and B which are dependent on the material used [8].

$$Z = A*\sinh*(B*\sigma/E)^{n} \tag{3-3}$$

During the initial development of the material model the data obtained from Chang were split in to two regions; consisting of SD creep and logarithmic creep [35]. To accurately develop a model, both of these regions were included in the original material model equation. The equation that relates to the logarithmic creep deformation regime is Equation 3-4 [8].

$$Z = C*e^{(D*\sigma/E)} \tag{3-4}$$

Equation 3-4 shows the Zener-Hollomon parameter equal to a material constant, C, multiplied by an exponential term, which includes a different material constant, D, and stress, σ, and Young's modulus, E. The right sides of Equations 3-3 and 3-4 are added to one another to account for both deformation regimes. This results in one single equation that can be set equal to the Zener-Holloman parameter that covers both SD creep and

logarithmic creep. This new equation is then used in conjunction with Equation 3-2 and results in Equation 3-5, where ε̇ is the strain rate. Equation 3-6 gives the change in strain rate over time and is equal to the derivative of Equation 3-5.

$$\dot{\varepsilon} = e^{-Q_c/RT} * dt*(A*(\sinh(B*\sigma/E)^n)+ C*e^{(D*\sigma/E)}) \ s^{-1} \quad (3\text{-}5)$$

$$\ddot{\varepsilon} = e^{-Q_c/RT} * dt*[(C*D/E)*e^{B*\sigma/E} + e^{-Q_c/RT} *dt \quad (3\text{-}6)$$

$$*(A*B*n)/E*\cosh(B* \sigma/E) *\sinh(B* \sigma/E)^{n-1}] \ s^{-2}$$

After running preliminary simulations it was determined that Equation 3-4 was not a significant contributor to the strain rate for the conditions of this study, which were more toward hot forming than warm forming. The Z values that were reached during the simulation bulge testing were not of a high enough value to be in the logarithmic creep range. As shown in Table 3-1 the percentages of the total strain rate, as well as strain rate values, are given for both the SD creep regime and the logarithmic creep regime. At the fastest strain rate, during the 450°C and 2410kPa simulation, the percentage of the total strain rate that is attributed to logarithmic creep is under one-fifth of one percent. This small percentage will not affect the forming time of the simulations and thus the logarithmic regime portion of the equation was removed from the final equation.

Temp (C°)	Pressure (kPa)	Zener Holloman Parameter	Strain Rate SD Creep	Strain Rate Log Creep	SD Creep % of Strain Rate	Log Creep % of Total Strain Rate
300	1380	2.90E+08	1.16E-04	6.85E-09	99.994%	0.006%
300	1724	3.85E+08	1.54E-04	7.98E-09	99.995%	0.005%
300	2069	8.23E+08	3.29E-04	1.61E-08	99.995%	0.005%
300	2410	1.54E+09	6.15E-04	4.97E-08	99.992%	0.008%
350	1030	4.93E+07	1.95E-04	4.60E-08	99.976%	0.024%
350	1380	1.75E+08	6.91E-04	5.63E-08	99.992%	0.008%
350	1724	4.53E+08	1.79E-03	8.79E-08	99.995%	0.005%
350	2069	1.02E+09	4.04E-03	2.18E-07	99.995%	0.005%
350	2410	2.23E+09	8.81E-03	1.43E-06	99.984%	0.016%
400	690	1.11E+07	3.08E-04	3.04E-07	99.901%	0.099%
400	1030	6.37E+07	1.77E-03	3.31E-07	99.981%	0.019%
400	1380	4.28E+08	1.19E-02	5.94E-07	99.995%	0.005%
400	1724	6.26E+08	1.74E-02	8.16E-07	99.995%	0.005%
400	2069	1.51E+09	4.19E-02	3.29E-06	99.992%	0.008%
400	2410	3.10E+09	8.62E-02	3.67E-05	99.957%	0.043%
450	690	1.51E+07	2.25E-03	1.65E-06	99.927%	0.073%
450	1030	8.44E+07	1.26E-02	1.84E-06	99.986%	0.015%
450	1380	2.85E+08	4.25E-02	2.54E-06	99.994%	0.006%
450	1724	7.84E+08	1.17E-01	5.63E-06	99.995%	0.005%
450	2069	1.67E+09	2.50E-01	2.30E-05	99.991%	0.009%
450	2410	4.28E+09	6.38E-01	1.02E-03	99.840%	0.160%

Table 3-1 Strain rate percentages of different mechanisms, SD creep and logarithmic creep, during preliminary bulge testing

It was also determined that after running the preliminary simulations using Equations 3-5 and 3-6 that the tensile data used to create these equations did not cover a wide enough range of Zener-Hollomon values to give an accurate representation of the experimental bulge testing. In Figure 3-1 the range of the original set of data is shown in a Log Z vs. Log σ/E plot.

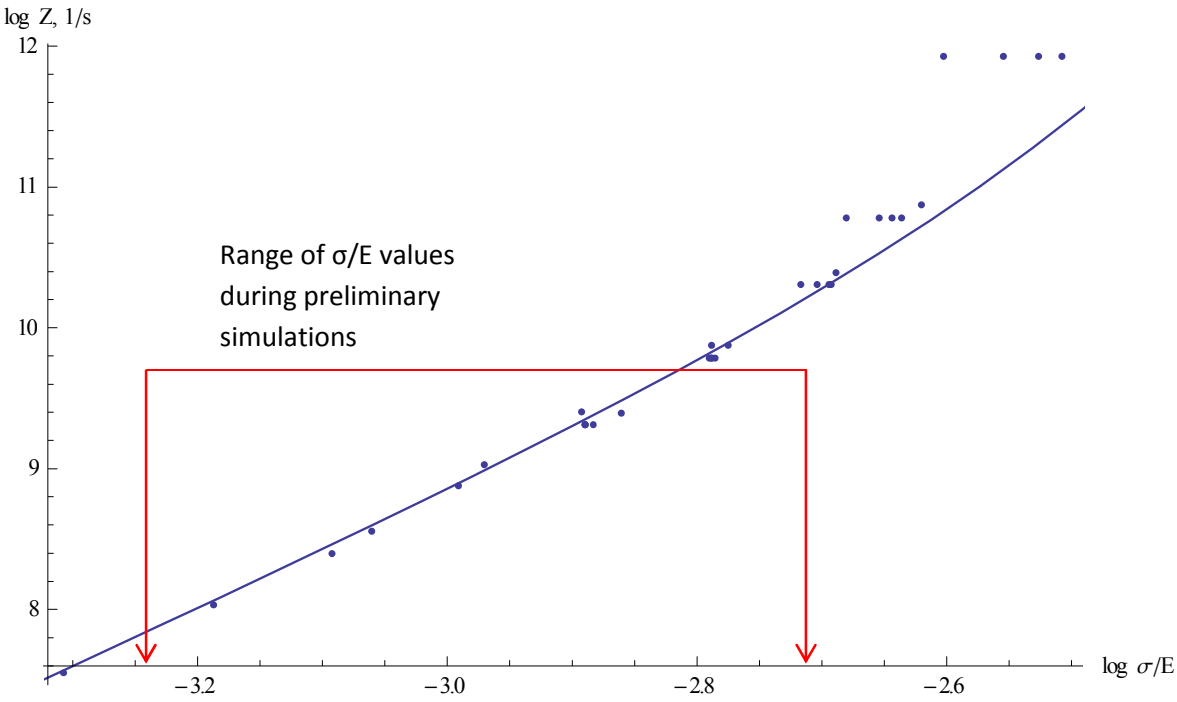

Figure 3-1 Plot of data taken by Brian Chang on a Log Z-Log σ/E [9]

As shown in Figure 3-1, there is very little data below $Z = 5*10^9\ s^{-1}$, and almost no data below $Z = 10^8\ s^{-1}$. When running the preliminary simulations, it was found that the range of Z values at the pole, where the strain rate is at the fastest and thus the Z value is at its highest, were $1.1*10^7 < Z < 4.3*10^9\ s^{-1}$. These values are also shown in Table 3-1. It was determined that the data from Chang alone would be insufficient to

determine an accurate material constitutive model. More data at much lower Z values, or slower strain rates, or higher temperatures, are needed.

Data for 5000-series alloys from a prior study by Taleff, Nevland and Krajewski [26] were added to the original data being used that were experimentally determined by Chang. The data from Taleff, et al, range from 150°C to 450°C and the Z values associated with these temperatures ranges from $3.2*10^{5}$ to $2.9*10^{17}$ s^{-1} [26]. This is a much more complete range of values that help create a more accurate material model to simulate the bulge testing using the ABAQUS™ finite element analysis. In Figure 3-2 the new data are plotted in the same format, log Z vs. log σ/E, along with the original data to give a much better fit.

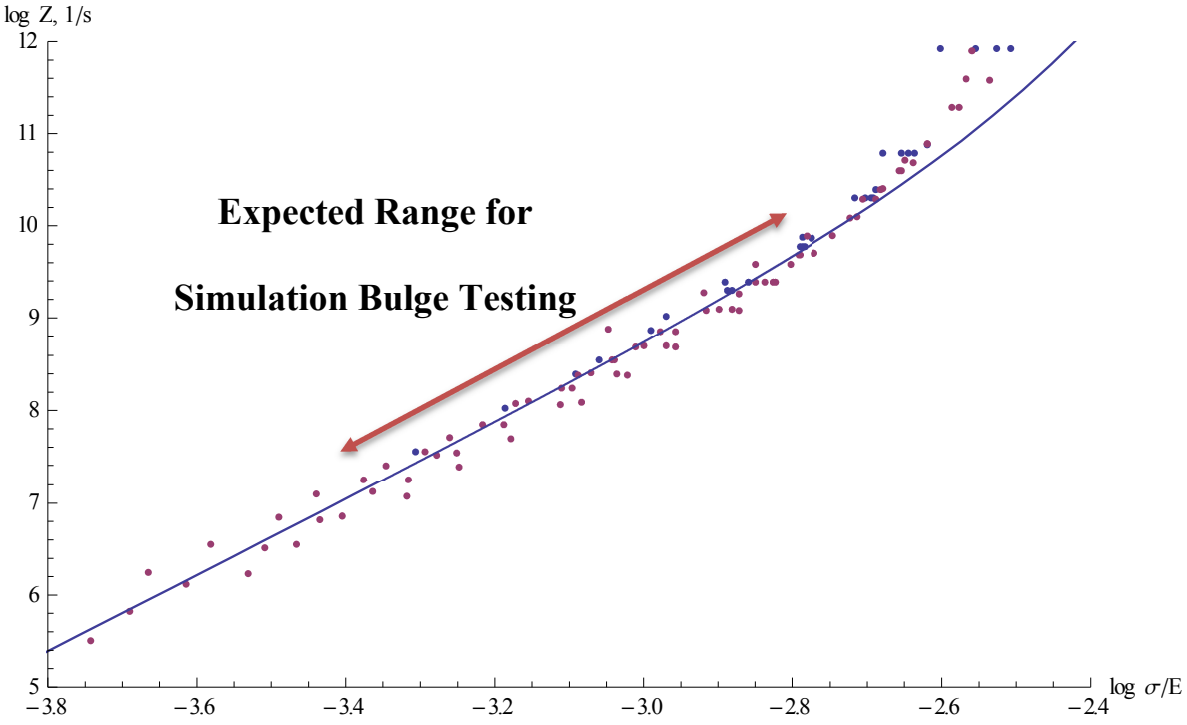

Figure 3-2 Sinh model fit on a Log Z vs. Log σ/E plot, showing expected range of simulation bulge testing values

As shown in Figure 3-2, there are more data points in the lower Z value range where the bulge simulation testing takes place. This additional data allowed for a newer more accurate material model equation to be determined.

The two separate curve fits shown in Figures 3-1 and 3-2 were obtained through the same method, by plotting the data as shown in the figures and fitting a curve to the data. Two different methods of fitting a curve were used to determine which method gave a better fit, and thus a more accurate model. The first fit that was used was a linear fit, which fit the data reasonably well at the lower end of the spectrum of Z values, but did not cover the higher Z values as well. The linear model was used while limiting the data to an appropriate region, where the maximum value of log σ/E is -3.0. The second fit was a non-linear fit, and a hyperbolic sine function was chosen. This equation used both the Z values and the σ/E values to select the appropriate data range for the model to fit. The maximum allowed Z value was $10^{10.5}$ s^{-1} and this corresponded to a maximum log σ/E value of -2.5. The hyperbolic sine equation, Equation 3-3, fit better than the linear fit. This was used while specifying the form of the non-linear model to be the same hyperbolic sine function in the form $A*\text{Sinh}(B\ \sigma/E)^n$, as Equation 3-3. This model was fit without using the logarithmic values of Z and σ/E. As shown in Figure 3-2, the hyperbolic sine function fits the data very well across the ranges that were specified. The fit tails off at the higher Z values, where logarithmic creep begins, but those values are not important to the bulge testing according to the preliminary simulations and the Z

values that those simulations predicted. The final equation for the material constitutive model shown in Figure 3-2 is:

$$\dot{\varepsilon} = e^{-Q_c/RT} * 9 * 10^9 * (\text{Sinh}(490.866 * \sigma/E)^{4.11}\ s^{-1} \quad (3\text{-}7)$$

This fit is much better than the linear fit, due to the slight upward curve towards the higher Z values.

3.2 Material Model Uncertainty

Now that a material model has been established, it is important to determine how accurate that model can be based on the possible error in the tensile data that were used to create the model. To determine the total amount of error between the tensile data and the fitted model, a method similar to root mean square was employed. The absolute error between each individual data point and the corresponding predicted point, at the same log σ/E value, on the fitted hyperbolic sine model, was calculated.

Figure 3-3 shows the absolute error in log Z vs. log σ/E to determine if there was any correspondence between the log σ/E values and the difference between the actual data point and the model.

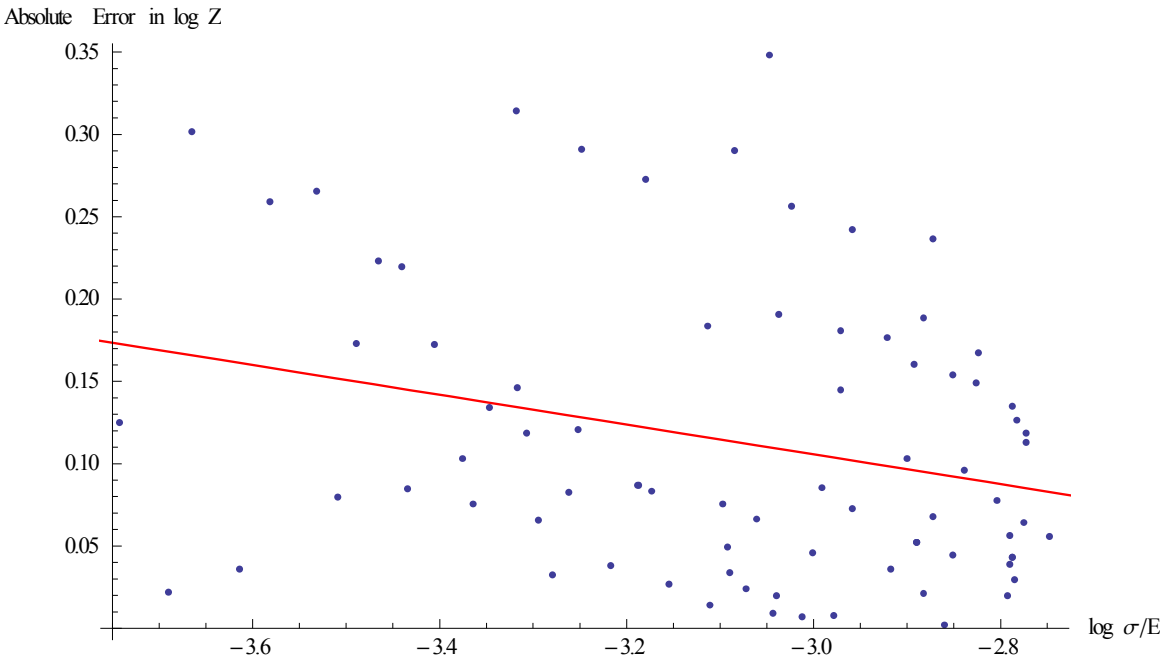

Fig 3-3 Absolute Error in log Z vs. log σ/E of a smoothed set of data

As shown in Figure 3-3, there is only a very weak correlation between the absolute error and the σ/E values. Since there is no significant correlation between the log σ/E values and the absolute error in log Z, it was determined that a constant error is the best way to quantify this with a statistical analysis. Since the error was calculated as an absolute value, the negative of each point was also added to create a symmetric data set of error values. Standard statistical analysis with a normal distribution was then used for this symmetric set of data, including defining a root mean square error. Fitting a normal distribution to the root mean square error shows that the standard deviation of the root mean square error is a good measure of uncertainty in the tensile data.

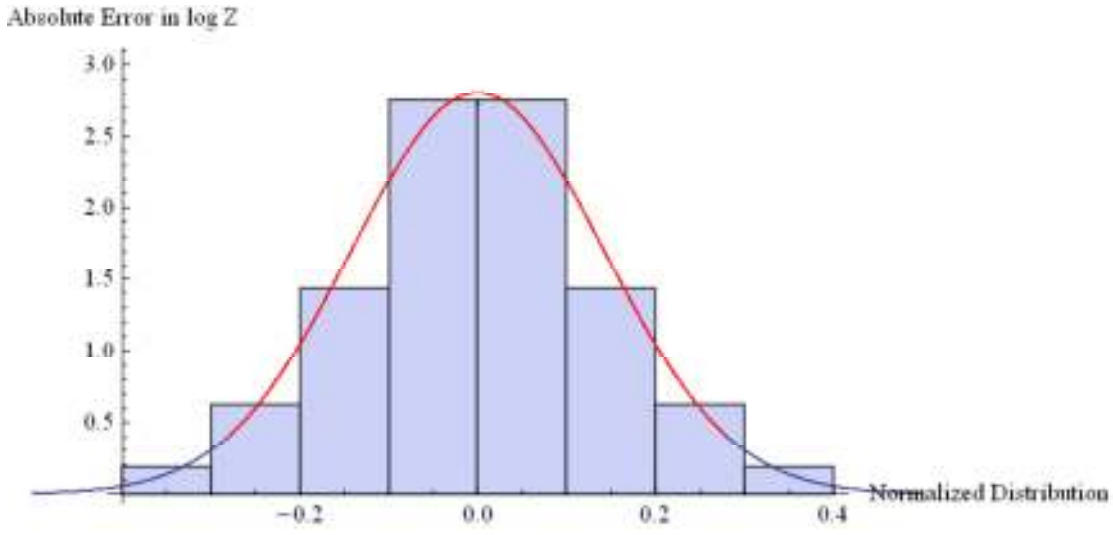

Fig 3-4 Histogram of the RMS Error Data. Red line indicates ±2 Standard Deviations

The standard deviation, see Figure 3-4, appears to be a very good measure of the uncertainty of the material model. The red line shown in the figure indicates a 95% confidence interval, which is slightly less than two standard deviations from the mean. The 95% confidence interval values will be used as the uncertainty for the material model, and two separate equations were created to bound this uncertainty. These high and low material models are shown as Equations 3-8 and 3-9, respectively. The only value that changes is the material constant A, while the constants B and n stay the same.

$$\dot{\varepsilon}_H = e^{-Q_c/RT}\ 1.249*10^{10}*(\sinh(490.866*\sigma/E)^{4.11}\ \ s^{-1} \tag{3-8}$$

$$\dot{\varepsilon}_L = e^{-Q_c/RT}\ 6.484*10^{9}*(\sinh(490.866*\sigma/E)^{4.11}\ \ s^{-1} \tag{3-9}$$

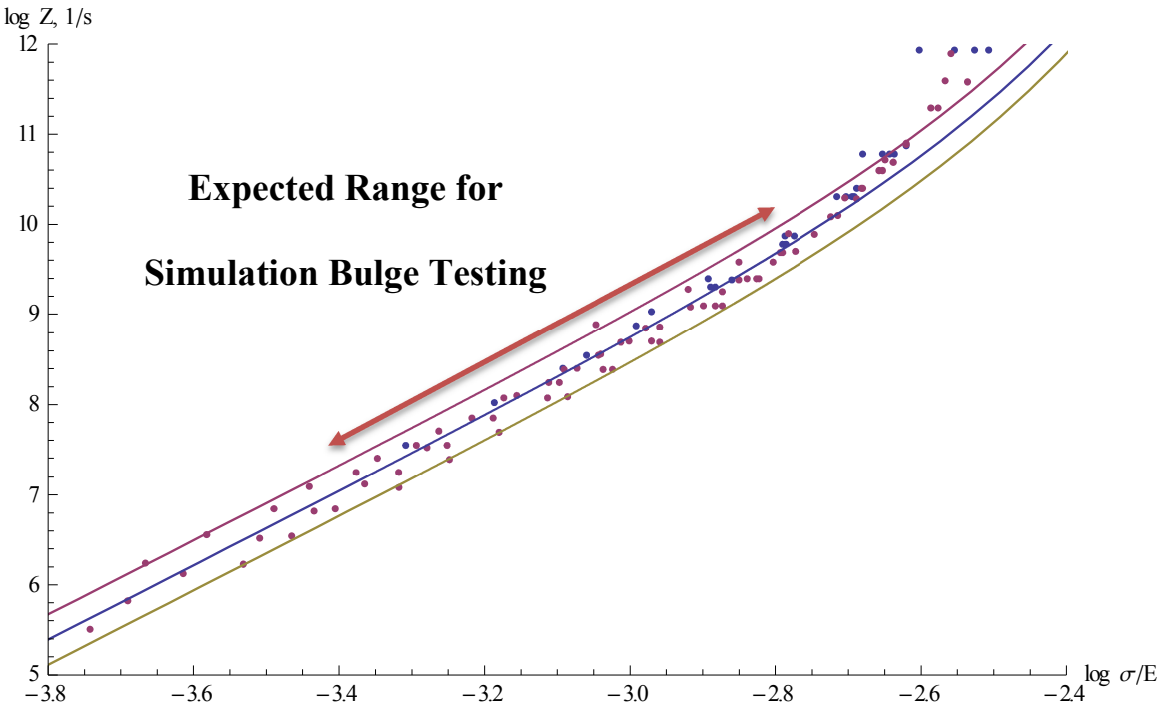

Figure 3-5 Material model with upper and lower 95% confidence intervals plotted with tensile data, also showing expected range for simulation bulge testing

These two equations create an upper and lower bound inside which the experimental test results should be contained, which is shown in Figure 3-5. As shown in the figure, the 95% confidence bands, the red and yellow curves, bound the data very well in the ranges that will be seen in the simulations. This suggests that the forming times for the experimental bulge testing should be within the limits set by these uncertainty bounds.

3.3 Material Model Verification

To verify that the material model will accurately predict the way the material should react to the stresses and temperatures that it will undergo, the model was used in

tensile test simulations. These tensile test simulations were run using the same finite element analysis program, ABAQUS^{TM}, as the bulge simulations were run. The mesh used for the tensile test simulations had 7 nodes running across the width of the tensile specimen, and 26 nodes running the length of the specimen. This was the same tensile test method used in previous simulations by Chang [9].

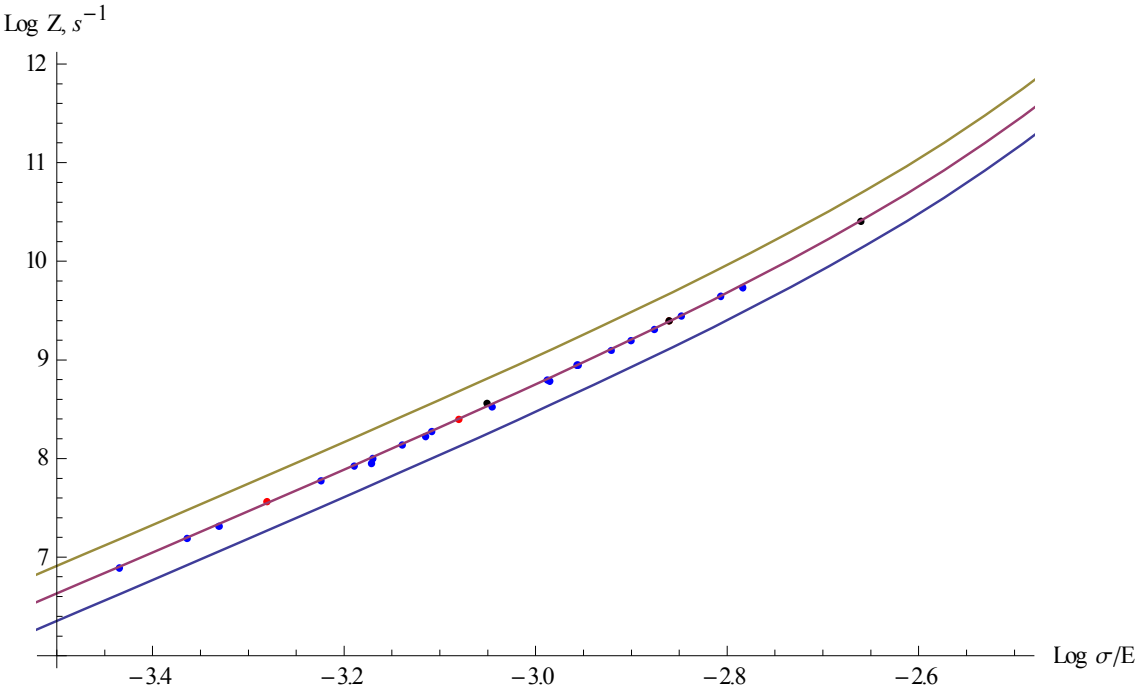

Figure 3-6 Material model curves plotted alongside tension test simulation values, which are shown as markers

Figure 3-6 shows tension simulation results using the material model outlined in Equation 3-7. These tensile test simulations were run at three different temperatures, 300°, 350° and 400°C, and two different true strain rates, .001 s^{-1} and .01 s^{-1}. As shown in the figure, the simulation results line up on the curve fit of the material model, which

shows that the material model was correctly implemented using ABAQUS^{TM}. The material model is now verified to work correctly.

Chapter 4: Experimental Results

4.1 Experimental Results and Adjustments

The aluminum alloy AA5182 that was used in this study was received in a sheet that was 1 mm thick from Furukawa-Sky Aluminum Corporation. The aluminum sheet was cut into 25 individual bulge specimens and tested using the equipment described in Chapter 2. Aluminum alloy AA5182 has a primary alloying element of magnesium at roughly 4.5 weight percent as well as some other minor alloying elements, none exceeding more than 0.5 weight percent individually [11]. Gas-pressure bulge experiments were run at temperatures ranging from 300°C to 450°C and at pressures ranging from 690 to 2410 kPa (100 psi to 350 psi). A maximum time for forming experiments was set at 40 minutes (2400 seconds) for each individual dome. The experiments were run using a single temperature per test, from the lowest to the highest temperatures in successive tests. The various tests at each temperature were conducted at the pressures in Table 4-1 in random order, to avoid any systematic errors in increasing pressure from one test to the next. After each test, the specimen was immediately taken out of the testing die and allowed to air cool.

As shown in Table 4-1, the maximum dome height was 25.7 mm, which is the limit of measuring capability, and each dome achieved a height of at least 10 mm. The specimen tested at 400°C and 1720 kPa ruptured suddenly and catastrophically. To avoid any damage to the test equipment from such ruptures, precautionary measures were added to stop each subsequent bulge at a dome height of approximately 20 mm.. In Table

4-1 the tests in italics were stopped due to reaching the maximum allotted amount of time, 40 minutes, while the tests in bold were stopped due to reaching the maximum dome height of 20mm.

. **Experimental Dome Height Results**

Temperature(C°)	Pressure(kPa)	Dome Height(mm)	Time to Test End(s)
300	*1380*	*11.5*	*2393.4*
300	*1720*	*12.8*	*2392.2*
300	*2070*	*12.6*	*2390*
300	*2410*	*14.1*	*2365*
350	*1030*	*13.6*	*2388.4*
350	**1380**	**23.9**	**2164.4**
350	**1720**	**24.9**	**940.2**
350	**2070**	**25.7**	**782**
350	**2410**	**25.6**	**417.2**
400	*690*	*16.7*	*2392.6*
400	**1030**	**23.8**	**805.8**
400	**1380**	**20.1**	**230.2**
400	**1720**	**25.7**	**111**
400	**2070**	**20.2**	**47.4**
400	**2410**	**20.4**	**20.6**
450	**690**	**20**	**505.4**
450	**1030**	**20.1**	**100.8**
450	**1380**	**20.2**	**34.8**
450	**1720**	**20.5**	**18**
450	**2070**	**20.7**	**8**
450	**2410**	**22.5**	**6.2**

Table 4-1 Dome height and test time at test end for all experimental bulge testing specimens. Tests in italics were stopped at a time of 40 min. Tests in bold were stopped at a dome height of 20mm.

Also shown in Table 4-1 is the time, in seconds, from the beginning of the test to the end of the test, whether that was due to reaching the maximum allowed dome height (20mm) or reaching the maximum allowed time (40min). As would be expected, the time to achieve a maximum dome height decreases as pressure and temperature increase. A total of six experiments reached the maximum time allowed. From Table 4-1, a desirable forming time for a practical application is that for which the maximum allowed dome height was reached in a relatively quick time, but not so fast as to preclude control of the forming process.

Figure 4-1 350°C 2070 kPa bulge experiment, photo take after 782 seconds of forming to a height of 25.7mm

A post-test bulge specimen, shown in Figure 4-1, tested at 350°C and 2070 kPa (300 psi) formed to a maximum height of 25.7mm in a little over 13 minutes. The sealing bead is clearly visible around the outer ring of the dome specimen. As shown in the figure, the dome has only a small rupture at its peak, which released gas pressure and ended the forming process.

Figure 4-2 Rupture at pole of the specimen tested at 350°C and 1720 kPa after a forming time of 940 seconds to a dome height of 24.9mm

In Figure 4-2 a dome tested at the same temperature of 350°C but at a lower pressure of 1720 kPa shows a large rupture at its pole. This dome reached a maximum

height of 24.9 mm before rupture. Rupture of the dome during solute-drag creep is likely a result of cavitation [34]. Once the material thins down to a significant extent, the cavities in the material can interlink and lead to through-thickness rupture. The rupture in the dome in Figure 4-2 is along the rolling direction, as would be expected. The reason that the material fails along the rolling direction is that the stringers of particles formed during rolling will guide cavity nucleation, growth and coalescence [34, 35].

During each bulge test, there was a small period of time at the beginning and end of each test where the data logger recording the bulge height of the dome was running and the gas pressure had yet to be applied, or had been shut off at the end of the test. This must be accounted for to accurately compare the experimental data among tests or to simulations.

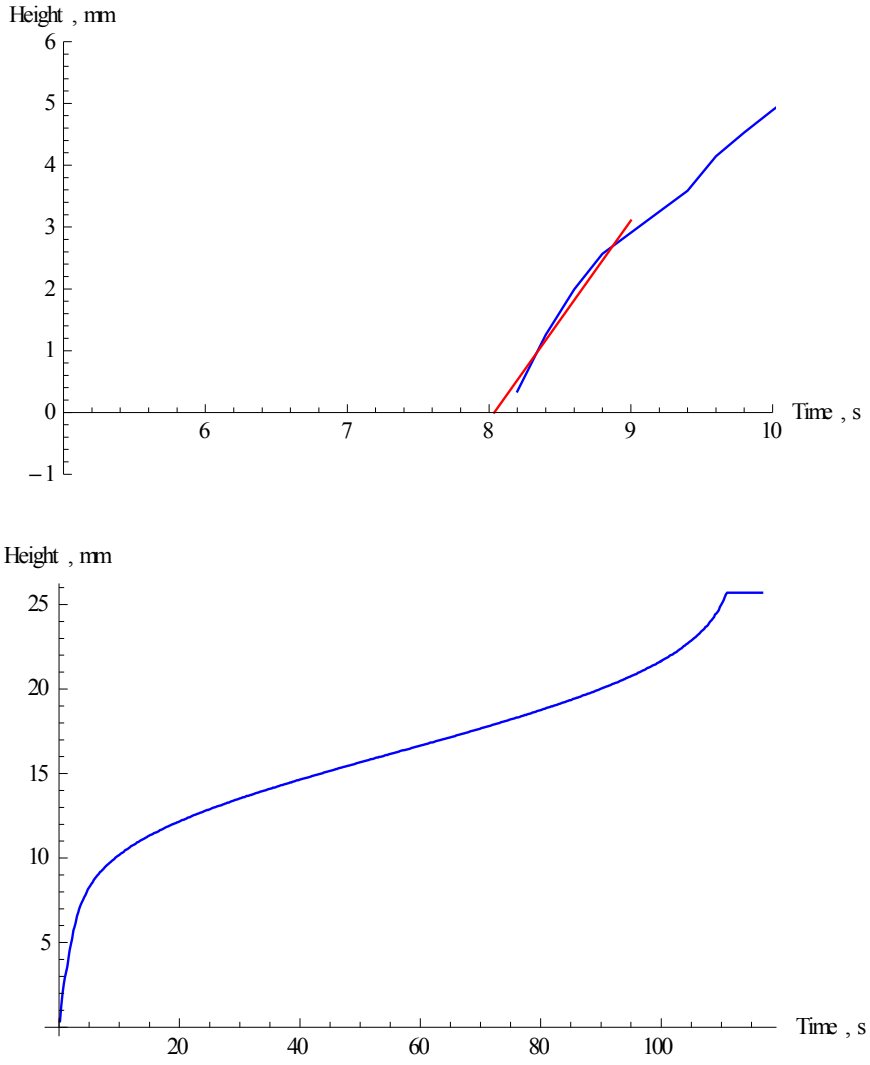

Figure 4-3 a) Linear fit time adjustment b) Final dome height vs. time graph post adjustments

As shown in Figure 4-3a above, the time period after the start of data logging and before the gas pressure was applied was roughly 8 seconds. For each test this time was different, and the data of each test was adjusted differently to ensure that an accurate start time for pressure application was enforced. The time to fully pressurize the chamber, which was discussed within the experimental procedures, was not considered in correction of the start time because at the lower temperatures and pressures this delay did

not make a significant difference in forming time, and at the higher pressures and temperatures there was no precise way to adjust for this difference. After the adjustments to the experimental data were made, data for each specimen were plotted with dome height, in mm, on the vertical y-axis and the test time, in seconds, along the horizontal x-axis.

4.2 Effects of Pressure and Temperature

Once all the experiments were complete, a comparison at a constant temperature was needed to see the effects of pressure on specimen forming. This is shown in Tables 4-1 and 4-2, but is illustrated more comprehensively in Figure 4-4.

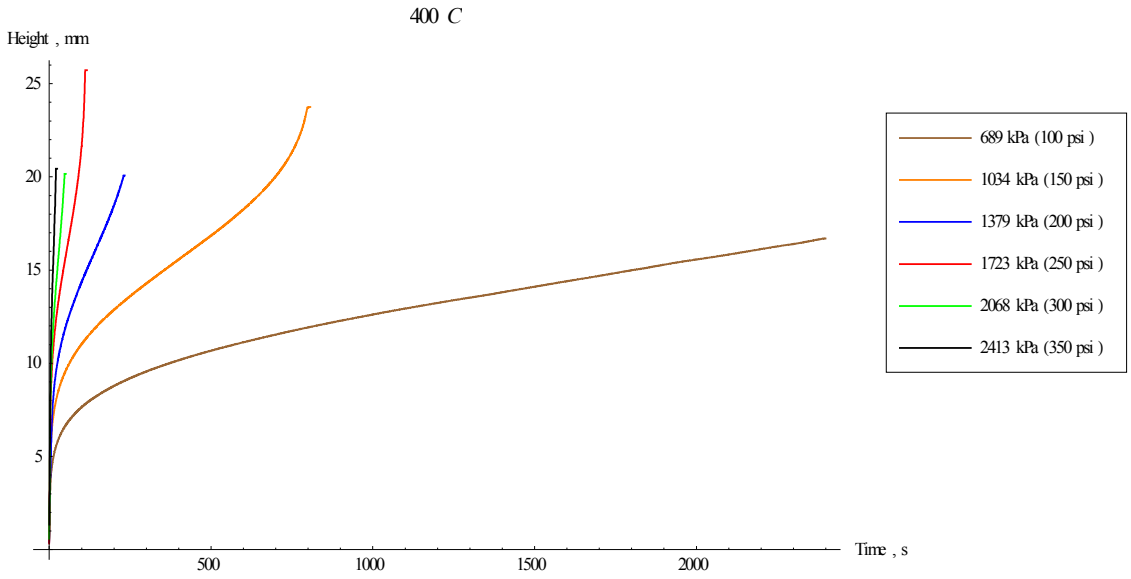

Figure 4-4 Dome height vs. time graph showing effect of forming pressure at 400°C for experimental tests

Figure 4-4 shows the effect of pressure on the forming rate at 400°C in a plot of dome height, in mm, vs. time, in seconds. The lowest pressure of 690 kPa is allowed to form for 2400 seconds and reaches a maximum dome height of less than 20 mm, which is less than every other sample at that temperature. The difference in final dome height between different pressures is significant at low temperatures but diminishes as the temperature increases. Due to the length of time over which the test at 690 kPa was conducted (influencing the scale of the graph's X-axis), it is difficult to see the difference between the highest three pressures, but these form very quickly. If each sample was compared at a dome height of 15 mm, the differences in forming time can be clearly seen across the various pressures. The specimen tested at 400°C and 1030 kPa shows 3 very distinct stages of deformation; initial, steady-state and final. The sample tested at 690 kPa shows only the first two stages, and does not have enough time to reach the final stage where the deformation rate once again increases.

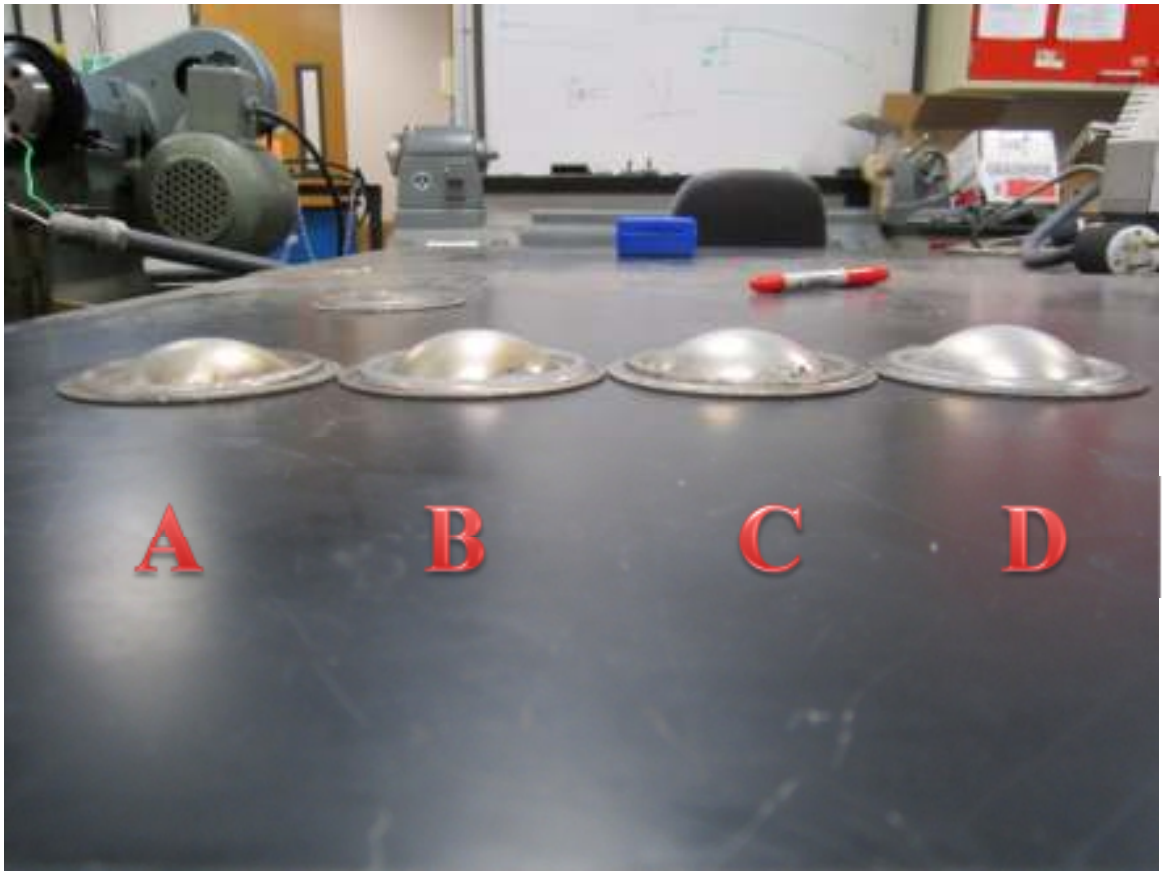

Figure 4-5 Samples tested at 300°C and a) 1380 kPa b) 1720 kPa c) 2070 kPa d) 2410 kPa, all tested to 2400s

Figure 4-5 shows four samples tested to the full time allotment, 2400 seconds, at 300°C and at various pressures. The four samples differ slightly in dome height with samples B and C in the figure being very close in dome height. Unlike the differences seen in Figure 4-4, where most of the samples reached the maximum height in under the allotted time, the lower temperature samples seen in Figure 4-5 were tested for the same time but show varying dome heights. This illustrates the temperature dependence of forming. Now that it has been shown experimentally that the pressure of the applied gas matters in forming time and dome height (shown in Figures 4-4 and 4-5 respectively),

there is the question of how much of an effect the temperature has on the forming time and dome height.

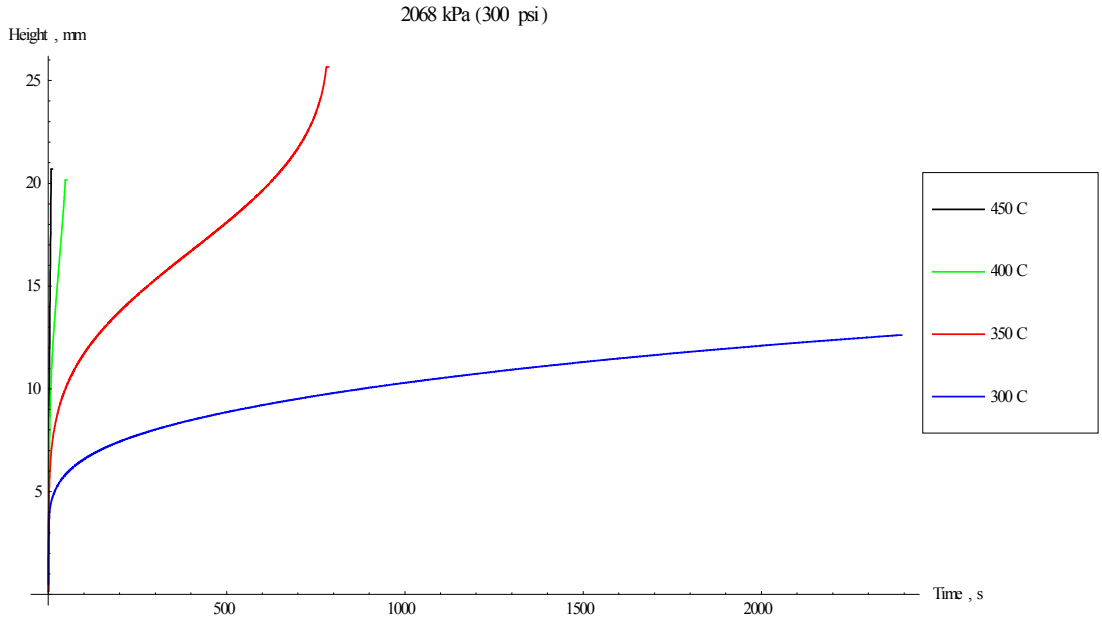

Figure 4-6 Dome height vs. time graph showing the effect of temperature at 2070 kPa

Figure 4-6 shows the effect of temperature at a constant pressure of 2070 kPa. The lowest temperature of 300°C only allows a dome height of slightly above 10 mm in 2400 seconds, while the higher temperatures allow dome heights of 20mm or greater. There is a significant increase in forming rate between 300°C and 350°C. This is evident in the slope of the 'steady-state' region of deformation and in the initial stages of forming as well. The 300°C test reaches a steady-state region but does not reach the third stage of deformation within 2400 seconds. If compared at a height of 10 mm, the 300° C test reaches that height in roughly 1000 seconds while the 350°C test reaches the same height

in less than 100 seconds. The 400°C and 450°C tests reach that height in roughly 5 seconds or less.

Chapter 5: Simulation Results

5.1 Simulation Results

The bulge test simulations were run using the ABAQUS^{TM} finite element analysis (FEA) software package [31] for the same conditions as used in the experiments. A total of 21 simulation conditions were examined. High and low (95% confidence band) material models were used for each simulation condition, along with the normal material model, to make a total of 63 simulations i.e., with three separate calculations for each of the 21 experimental conditions. The dome heights and forming times were extracted from simulation outputs and are shown in Table 5-1.

Simulated Bulge Test Results

Temperature(C°)	Pressure(kPa)	Dome Height(mm)	Time at Test End
300	*1380*	*9.6*	*1800*
300	*1720*	*11.9*	*1800*
300	*2070*	*14.6*	*1800*
300	*2410*	*18.8*	*1800*
350	*1030*	*12.2*	*1800*
350	*1380*	*19.4*	*1800*
350	**1720**	**24.8**	**957**
350	**2070**	**24.6**	**429**
350	**2410**	**24.4**	**213**
400	*690*	*16.3*	*1800*
400	**1030**	**24.8**	**977**
400	**1380**	**24.5**	**286**
400	**1720**	**24.7**	**109**
400	**2070**	**24.6**	**48.9**
400	**2410**	**24.7**	**24.5**
450	**690**	**24.6**	**513**
450	**1030**	**24.4**	**146**
450	**1380**	**24.3**	**43**
450	**1720**	**24**	**16**
450	**2070**	**24.5**	**7**
450	**2410**	**24.6**	**4**

Table 5-1 Simulated bulge testing dome heights at test end. Test simulation runs in italics reached the maximum allowed time of 1800 seconds. Test simulation runs in bold reached the maximum allowed dome height of 25 mm.

There are no simulated dome heights over 25 mm, and this reflects the dome height measurement limit of the experimental tests; once the dome height of the simulation reached, this defined maximum dome height of 25 mm, any subsequent deformation was ignored. Simulated dome height values in Table 5-1 above were taken at either 1800 seconds of testing or when the dome height reached 25 mm, whichever occurred first. The simulation results shown in italics reached the maximum allowed simulation time of 1800 seconds, and the simulation results shown in bold reached the maximum allowed dome height, 25 mm. Most of the simulations reached the maximum allowed dome height, with only one third of the simulations failing to reach the maximum allowed height within the maximum allowed simulation time of 1800 seconds. None of the simulations at the lowest test temperature, 300°C, reached the maximum allowed dome height, and it is not until 450°C that the lowest pressure, 690 kPa, produced the maximum dome height before reaching the maximum allowed time.

5.2 Effects of Pressure and Temperature

The effects of increased temperature and pressure on simulation predictions are evident in Table 5-1. As the temperature increases, the time required to reach a particular dome height decreases. This is due to the softening that occurs as the temperature increases [7]. As shown in Equation 3-5, as temperature increases so does the plastic strain rate. At a constant pressure of 2070 kPa (300 psi), the time required to form to a dome height of 24.6 mm at 400°C is approximately $1/9^{th}$ that required to form to the same dome height at 350°C.

The time to reach the maximum allowed dome height decreases as the pressure increases. This effect is shown in Equation 5-1 and the final material model, Equation 5-2. The stress is directly related to the pressure through Equation 5-1, which is the equation for a thin-walled pressure vessel.

$$\sigma=(p*r)/(2*t) \tag{5-1}$$

$$\dot{\varepsilon} = 9*10^{9}*(\text{Sinh}(490.866*\sigma/E)^{4.11} \quad s^{-1} \tag{5-2}$$

Comparing two simulated bulge tests at a constant pressure shows the importance of pressure on forming time. A simulated bulge test at 400°C and 2410 kPa (350 psi) forms roughly 4 times faster than a simulated bulge test at 400°C and 1720 kPa (250 psi). At a temperature of 450°C, a forming pressure above 1380 kPa (200 psi) produces an extremely fast forming rate, which could be fast enough to cause problems in real-world applications of forming.

5.3 Bulge Dome Stresses During Simulation

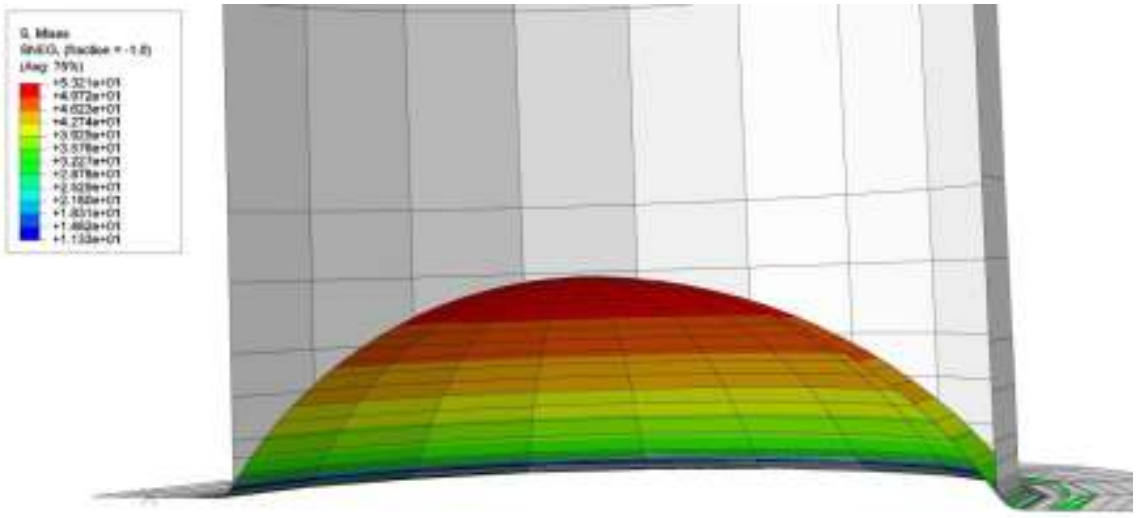

Figure 5-1 Simulation bulge testing specimen after 1800 seconds at a dome height of 14.6 mm at a condition of 300°C 2070 kPa

Figure 5-1 shows the image of a simulated bulge dome formed at 300°C and 2070 kPa at a dome height of 14.6 mm after the maximum test length of 1800 seconds. The stresses in the dome, during this stage of forming, are also shown and increase towards the pole. The die is shown in the background as all white and is held static throughout the simulation. The highest stress is at the pole, and the stresses decrease towards the edge of the test specimen, as would be expected during forming of a bulge specimen. The pole is the thinnest part of the bulge specimen, and Equation 5-1 for the stress in a thin-walled pressure vessel tells us that this will produce the highest stress. The stress at any point around the circumference of the dome is essentially invariant as a result of the axisymmetric nature of the bulge dome.

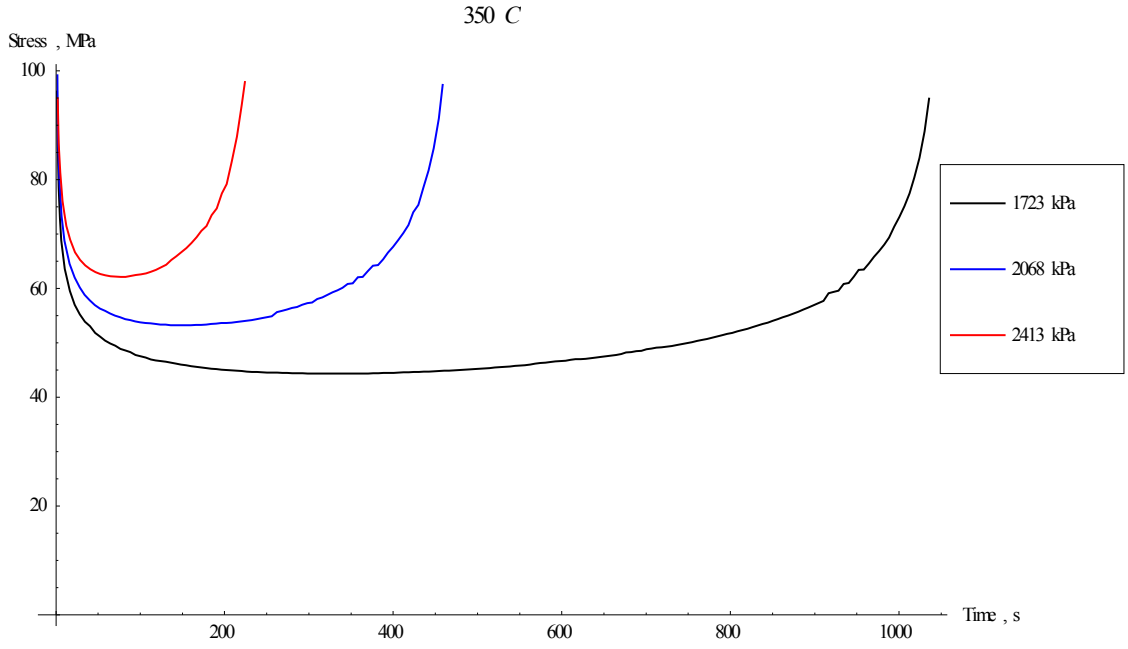

Figure 5-2 Plot of Stress, MPa, vs. Time shown for 3 conditions at a temperature of 350°C and pressures of 1720 kPa, 2070 kPa and 2410 kPa

As shown in Figure 5-2, the stresses during the test stay fairly constant for the majority of the applicable test time, only being higher at the very beginning and the very end of the test when the simulation has broken down and is no longer representative of real world behavior. The highest values of stress in Figure 5-2 are at the beginning of the test, when the radius of curvature is very large, and the end of a test, when the thickness of the bulge specimen is small. A comparison of the three simulations in Figure 5-2 shows increasing stress as the pressure is increased, as is expected from Equation 5-1.

5.4 Simulation Adjustments

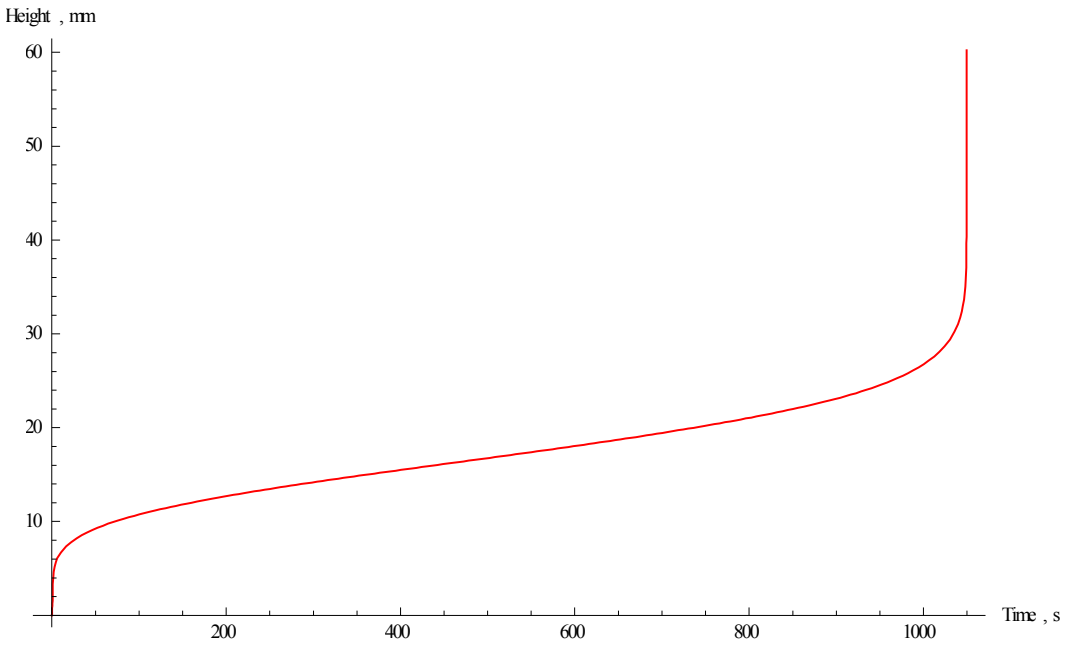

Figure 5-3 Simulation bulge testing dome height vs. time graph 350°C 1720 kPa

Figure 5-3 shows dome height, in mm along the y-axis, vs. time, in seconds along the x-axis, for a specimen that was tested at 350°C and 1720 kPa (250 psi). Figure 5-3 shows how, at test end, the dome height increases beyond what is reasonable in a very small amount of time. This is due to excessive thinning negatively affecting the simulation. The simulation does not account for failure mechanisms, such as cavity nucleation, that occur in the experimental bulge forming. Thus, the material thins to a greater extent than is possible in experimental bulge tests. This is one reason for the maximum imposed bulge dome height of 25 mm. A bulge dome height of 25 mm is also close to the real world maximum bulge dome height of these specimens.

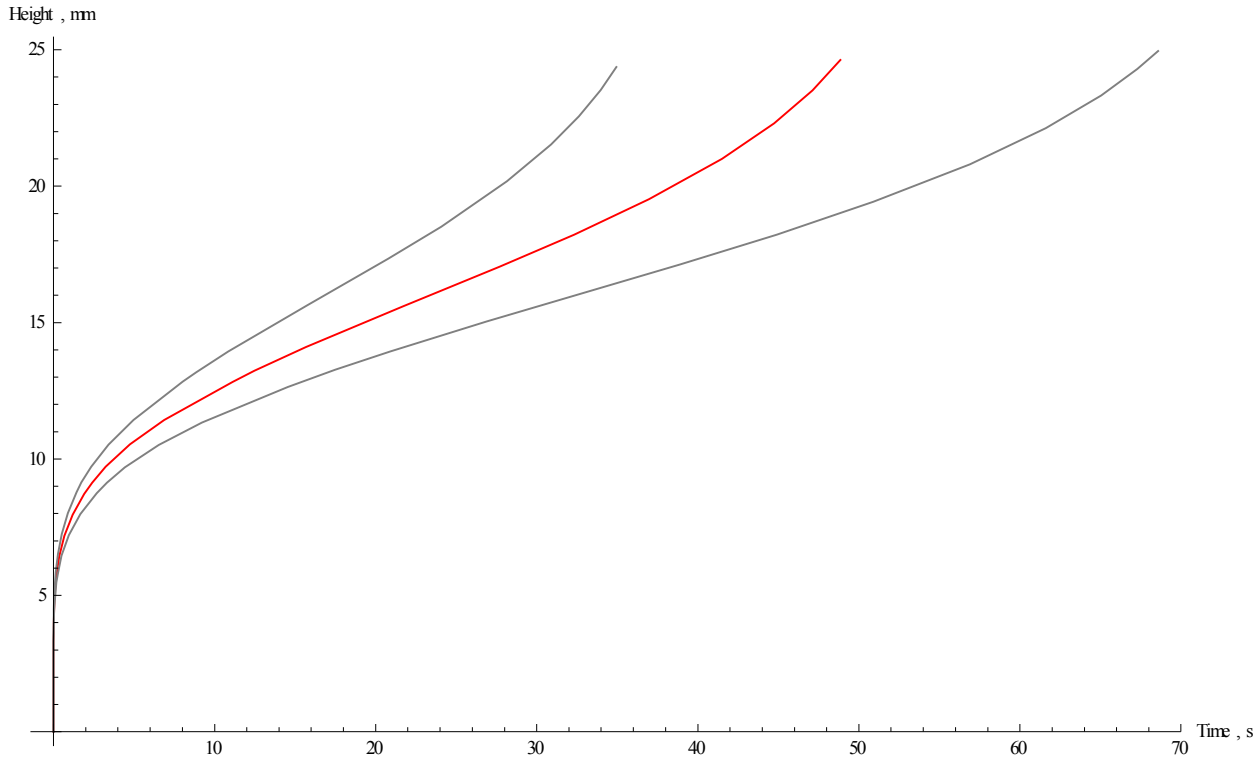

Figure 5-4 Graph of Dome Height, mm, vs. Time, s, the Simulation with ± 95% Confidence Intervals at a testing condition of 400°C and 2070 kPa

Figure 5-4 shows a plot of dome height, in mm along the y-axis, vs. time, in seconds along the x-axis, of a simulation with data up to the maximum allowed dome height of 25 mm. There are three separate curves shown in Figure 5-4, representing the predicted forming as well as the predicted uncertainty bounds. The red curve shows the simulation that used the material model Equation 5-2. The two gray curves represent the simulation predictions of the uncertainty bounds that used Equations 3-8 and 3-9. Comparing the simulations to the experimental data will show in what ranges of conditions the material model works well and in what ranges it may not work well.

Chapter 6: Comparisons of Results and Other Analyses

6.1 Comparison of Simulation and Experimental Results

Determining the accuracy of the material constitutive model requires evaluation of how well the model will predict the process of forming at different test conditions. One of the main goals of this study was to construct a model that would not only predict dome height of the material after forming, but also the dome height at any given time during forming. The material constitutive model gives an accurate prediction across multiple temperatures and pressures of the bulge dome height and forming times for a wide range of dome heights and forming times. Being able to accurately predict the forming time required to reach a variety of bulge dome heights allows for versatile real-world use of the material constitutive model.

Figure 6-1 shows a comparison of four experimental bulge tests with their respective simulations and 95% confidence bands. The comparisons are shown at a constant pressure of 1380 kPa (200 psi) and at temperatures ranging from 300°C to 450°C. The experimental test is shown in red, simulation prediction is shown as the solid black line and the uncertainty (95% confidence bands) is shown as the dashed black lines.

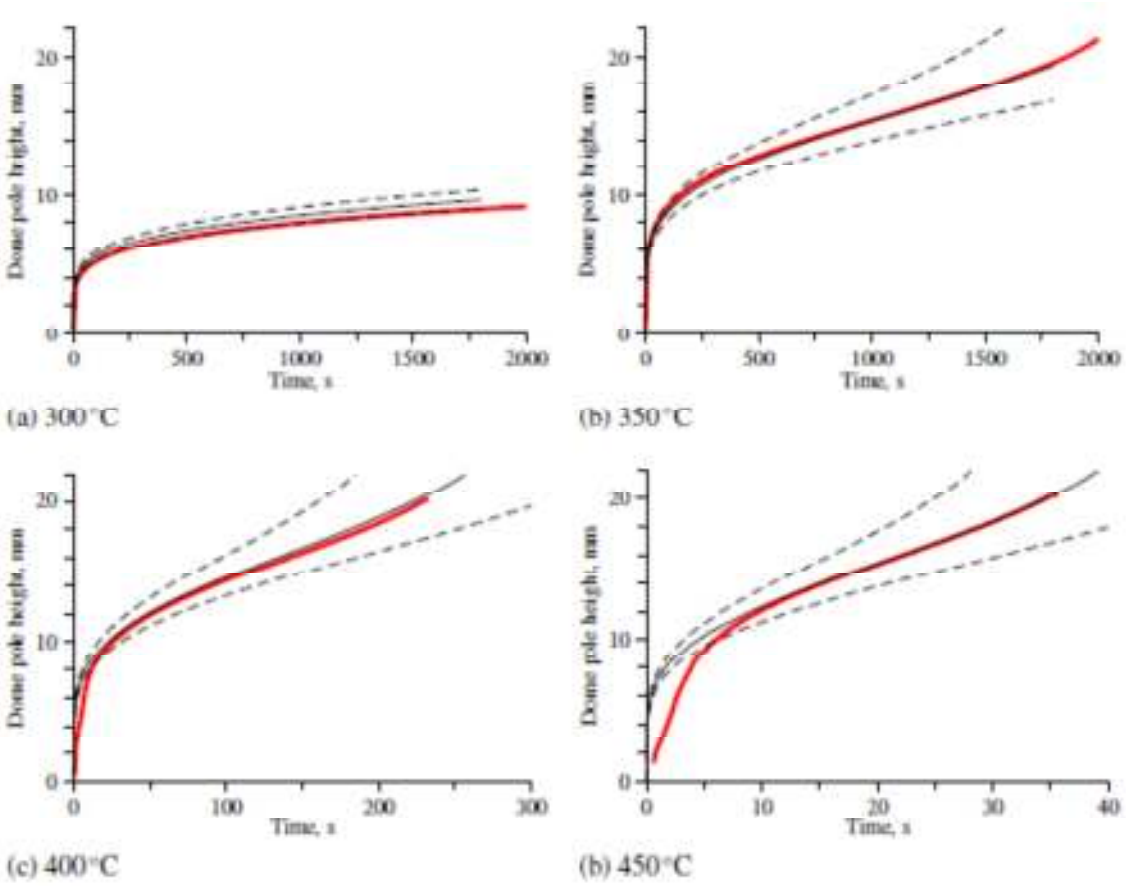

Fig 6-1 Comparison of simulation and experimental bulge tests at 1380 kPa and a) 300°C b) 350°C c) 400°C and d) 450°C. Experimental data are shown as the dark red curve, while the simulation prediction is the solid black curve and the 95% confidence bands of the simulation prediction are shown as the dashed black lines, taken from Predicting Hot Deformation of AA5182 Sheet by Lee et al.

As shown in Figure 6-1 the simulation runs follow the experimental tests very well, with near complete agreement in the 350°C, 1380 kPa test. As shown in Figure 6-1c and 6-1d, there is a slight disagreement at the very beginning of the experimental test.

The reason for this disagreement is due to the pressurization time of the chamber. As mentioned earlier, there was a lag in time between the valve opening to allow the gas to the top tube assembly and the time when there was full pressure throughout the die chamber. The time for this to occur was roughly 4 to 5 seconds and is more evident at the highest pressures and temperatures due to the scaling of the bulge dome height vs. time plots. The simulations do not account for this pressurization time. Despite this small disagreement, once the 400°C and 450°C bulge test experiments reach roughly 12 mm of bulge dome height, the simulations predict the bulge forming very well. However not all of the simulations and experiments agreed as well as those tested at a pressure of 1380 kPa. Some of the largest disagreements are shown in Figure 6-2.

Figure 6-2 shows four experiments and test simulations at four different test conditions, with the red line showing the experimental test, the black line showing the simulated test and the dashed lines showing the uncertainty bounds. Figures 6-2a and 6-2b show experimental and simulated tests at a temperature of 300°C and at pressures of 2070 kPa and 2410 kPa, respectively. Figures 6-2c and 6-2d show experimental and simulated tests that were tested at a temperature of 350°C and at pressures of 2070 kPa and 2410 kPa, respectively

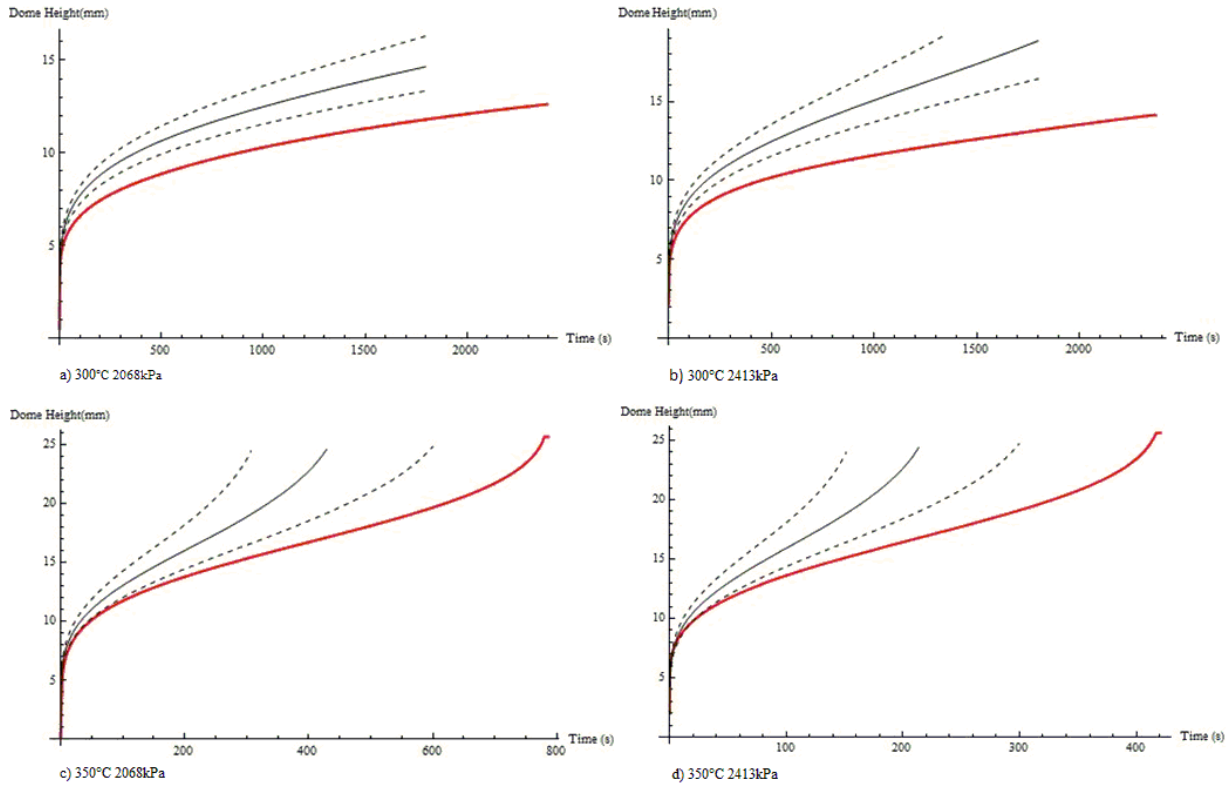

Figure 6-2 Comparison of simulation and experimental bulge tests at varying pressure and temperatures a) 300°C 2070 kPa b)300°C 2410 kPa c) 350°C 2070 kPa and d)350°C 2410 kPa. Experimental data is shown as the dark red curve, while the simulation prediction is the solid black curve and the 95% confidence bands of the simulation prediction are shown as the dashed black lines.

Each simulation shown in Figure 6-2 forms at a faster rate than the experimental test. The overall dome heights are in agreement, but the forming times differ. The simulations and experiments show some agreement at the initial formation stages up to roughly 10 mm, but then diverge near the "steady state" deformation region (where dε/dt is nearly constant). The reason for this divergence is due to strain-hardening (work-hardening). Strain-hardening occurs when new dislocations are created during plastic deformation, effectively hardening the material and making it more resistant to

deformation [1]. During the bulge testing, the material becomes harder as it is being formed slowing the rate of formation. Strain-hardening was not taken into account in the material model because there was no evidence of strain-hardening in the tensile data that was used in creating the material model.

Temperature(C°)	Pressure(kPa)	Average Effective Strain Rate s^{-1}
300	2070	2.80E-02
300	2410	1.62E-01
350	2070	3.67E-01
350	2410	6.13E-01

Table 6-1 Average Strain Rates of 4 simulated tests

Shown in Table 6-1 are the average effective strain rates at dome poles for the four tests, shown in Figure 6-2, where the simulation predictions and experimental data do not agree. These rates are generally faster than those for which tensile data are available. The fastest strain rate of tensile tests used for constructing the material model was 1.0*E-02 s^{-1}. Strain-hardening is not evident in the tensile tests because of their slow strain rates; however at these faster strain rates strain-hardening is evident in the experimental bulge specimens. Chang, et al, observed that strain-hardening does occur as temperature decreases and strain rate increases, but showed that this does not necessarily adversely affect tensile ductility during warm working [9]. This explains why the experimental tests still reached the maximum dome height of 25mm. The strain-hardening is not seen at the higher temperatures due to an offsetting softening of the material due to the increase in temperature; this is seen in the 400°C and 450°C experimental tests [7].

6.2 Error Analysis

After visually comparing the graphs of the simulations and experiments, a quantification of these errors was needed. The root mean square (RMS) and mean-percent difference (MPD) errors were then calculated. The equations used to calculate the RMS and MPD errors are shown below in Table 6-2.

Error Measure	Root Mean Square(RMS)	Mean Percent Difference(MPD)
Equation	$\sqrt{\frac{1}{n}\sum_{i=1}^{n} e_i^2}$	$\frac{1}{n}\sum_{i=1}^{n} \frac{e_i}{h_i^e} * 100$

Table 6-2 Equations used to calculate RMS and MPD Error

In Table 6-2 above n = 100, h_i is the height of the experimental bulge dome, e_i is the error in predicted dome height, which is the predicted height minus the experimental dome height at a given time. Linear interpolation was used to determine the dome height values for the simulated tests at the times used in the error analysis. The root mean square error gives an absolute value of error and does not tell in which direction the error lies. The mean percent difference, however, will give a positive or negative value based upon whether the simulation predicts faster or slower forming. A positive MPD error indicates that the simulation predicts a higher bulge dome height, faster forming, than the experimental bulge dome height and a negative MPD error predicts a lower simulation bulge dome height than the experimental bulge dome height. The RMS and MPD error values are shown in Table 6-3.

Temperature(C°)	Pressure(kPa)	Dome Height(mm) RMS Error	Dome Height MPD Error
300	1380	0.51	7%
300	1720	0.87	10%
300	2070	2.13	21%
300	2410	3.54	29%
350	1030	0.72	-7%
350	1380	0.17	-1%
350	1720	0.32	0%
350	2070	3.34	19.%
350	2410	3.40	20%
400	690	0.80	5%
400	1030	0.68	-2%
400	1380	0.55	4%
400	1720	0.59	3%
400	2070	2.13*	21%*
400	2410	2.08*	21%*
450	690	1.74	9%
450	1030	1.13	-5%
450	1380	1.15	10%
450	1720	3.35*	43%*
450	2070	4.90*	111%*
450	2410	9.17*	190%*

Table 6-3 Dome height error analysis, between simulated bulge testing and experimental bulge testing. Asterisk indicates inflated error values due to short test span.

Shown in Table 6-3 is the error for all test conditions. Table 6-3 also shows that for most of the simulations the RMS error between the simulated dome height and the experimental dome height is reasonably low. However, there are a few exceptions. This is the same case for the MPD error, where most of the cases are under 15% error. Some of the exceptions where the error is not small are the 4 simulations conducted at the two lowest temperatures, 300°C and 350°C and at the pressures of 2070 kPa and 2410 kPa. In these four tests, shown in Figure 6-2, the forming rates do not match up well with the predictions yielded by the simulations due to the strain-hardening that the material is seeing during the test. The other exceptions, (indicated with an asterisk in Table 6-3) where the errors are inflated is due to the short time span of the test. The problem with calculating the error for these cases is that with such a small total test time there is a significant amount of importance placed on the very beginning of the test, which at these conditions is significantly affected by the pressurization time. As shown in Figure 6-1d, there is a time at the beginning of the test where the experimental dome height is much lower than the simulation due to the non-instantaneous pressurization of the die during experimental testing. This causes a massive amount of error at the beginning of the test, which creates an unreasonable amount of total error. As shown in Figure 6-1d, after roughly 10 seconds the experimental data and simulation data follow each other closely; however, looking at the RMS error alone gives a much different picture. This is exacerbated for some of the higher pressure tests at 450°C, where the total test time is only a few seconds. The tests at the highest pressures and temperature form too quickly for a realistic dome height error analysis to be done.

6.3 Anisotropy

After numerically determining the error for the test conditions, there was a need to determine if there were other factors contributing to the error or if it could mostly be attributed to the scatter of the tensile data around the material constitutive model fit. One of those contributing factors could be plastic anisotropy, which is when the material is directionally dependent and the direction of stresses and strains affects the way the material forms [1]. If the samples that were being tested experimentally had different properties through the thickness of the material than in the sheet plane, then this would be important to know in trying to predict forming. Using tensile samples tested by Brian Chang [9], the plastic anisotropy was measured to determine if the AA5182 sheet, which was from the same stock as that used for these bulge test experiments, was anisotropic in the sense of normal plastic anisotropy.

Table 6-4 shows the test conditions and the R values of specimens tested by Brian Chang [9] under tensile loading. The R value was calculated by taking the strain in the width direction of the tensile specimen and dividing that by the strain in the thickness direction. An R value of 1 show that both the width and the thickness of the specimen were thinned at the same rate and that the material is isotropic.

Temperature(C°)	Strain Rate	Average R Value
300	$1x10^{-3}$	0.8
300	$3x10^{-2}$	0.8
300	$1x10^{-2}$	0.8
300	$3x10^{-3}$	0.8
350	$1x10^{-3}$	0.9
350	$3x10^{-2}$	0.6
350	$3x10^{-3}$	0.9
350	$1x10^{-2}$	0.9
400	$1x10^{-3}$	0.8
400	$3x10^{-2}$	0.8
400	$1x10^{-2}$	0.9
400	$3x10^{-3}$	0.9

Table 6-4 Anisotropy values of tensile tests previously tested by Brian Chang [9]

The values shown in Table 6-4 show that the material was thinned only slightly more in the thickness direction than the width direction. An R value higher than one would prove that the thickness direction is harder than the width direction and would not thin as quickly during a tensile test. When transferring this knowledge to a bulge test, a material that has an R value of much higher than 1 would form slower than a material with an R value closer to 1. This is due to the fact that as the x and y directions of a sheet are stretched it must thin out through the thickness of the material.

6.4 Shape Comparison

Determining the shape of the test specimen was another area of interest during this study. While the dome height is very important, if the simulated and experimental dome shapes are not similar then the simulations are not useful. Determining the shape of the simulated domes was done by outputting the nodes that make up the wire mesh and using the x and y coordinates to plot the nodes on a grid. The shapes of the experimental domes were examined by using an abrasive wheel to cut the domes through the pole. The domes were scanned in as a picture file at 1200 dots per inch. The experimental domes were taken at the point of test end, while the coordinates of the nodes in the simulated tests were extracted when the simulated bulge dome height matched that of the experimental dome height. This ensured that the experimental and simulated bulge tests were being compared at the same bulge dome height.

Figure 6-3 Cross section of experimental bulge test specimen tested at 300°C 1380 kPa showing points taken for shape comparison with simulated bulge tests. The scale shown on the bottom of the figure is in mm.

Figure 6-3 shows a scanned image of the cross section of the experimental bulge test at 300°C and 1380 kPa (200 psi). After scanning the image to a computer, coordinates were taken, starting at the dome pole, every 5 mm for 25mm on each side

along the x-axis. The range of the points taken along the x-axis is roughly the equivalent of the specimen diameter. A 152mm (6 inch) scale was used to measure out the 5 mm spacing between each measurement. The nodes of the simulated bulge test are at the center of the thickness of the material. To keep consistent with where the data points were taken in the simulated bulge specimens, at each of the 11 points along the x-axis a coordinate was measured on the outer and inner surfaces of the experimental bulge dome. This resulted in 2 y-coordinate values for every x coordinate, which were then averaged to find the center point of the thickness of the bulge dome. Once all of the data points for the experimental values were taken, and y-coordinates averaged, they were compared to the simulation data.

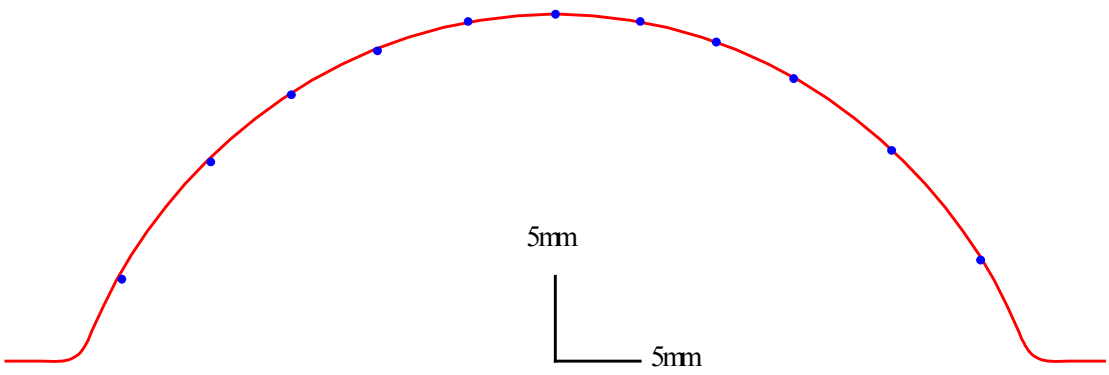

Figure 6-4 Shape comparison at a constant dome height of 20.4mm showing experimental bulge data points as blue dots, and simulated test as a red line from a condition of 400°C 1030 kPa

Figure 6-4 shows a comparison of experimental and simulated dome shapes that were tested at 400°C and 1030 kPa (150 psi). The blue dots shown in Figure 6-4 are the coordinates that were taken from the experimental specimen, and the red line shows the nodes of the simulated test. These were compared at the same dome height of 20.4 mm,

so that the pole point and the pole node in the simulation occur at the same point on the x-y grid. As shown in Figure 6-4 the blue dots are very close to, if not directly on top of the red line. This indicates that the shape of the simulated tests and the experimental tests are nearly identical. The experimental bulge dome height, as well as the shape of the specimen, is accurately predicted by the simulations. This shows that the model that was developed does an excellent job of determining the way the material will react in the conditions that were tested; excluding the conditions where strain-hardening was significantly involved.

6.5 Microstructure Analysis

The final step in looking at the experimental dome specimens was to determine if there was any abnormal grain growth during bulge forming. Static abnormal grain growth (SAGG) was found by Alex Carpenter after tensile testing of AA5182 at elevated temperature and a subsequent annealing [32]. To determine if this would occur during forming in biaxial bulge specimens two samples were taken and cross sectioned; one that was tested at 400°C and 2070 kPa (300 psi) and the other tested at 450°C 2070 kPa (300 psi). Three different areas of each experimental bulge sample were taken to look for grain growth. The three areas that were cross sectioned to determine grain growth were the pole, midway between the pole and the base of the dome, and the edge of the sample that was near the sealing bead and did not see the forming pressure. The edge of the sample was taken so that there would be a comparison that was not under the biaxial bulge stress during the test.

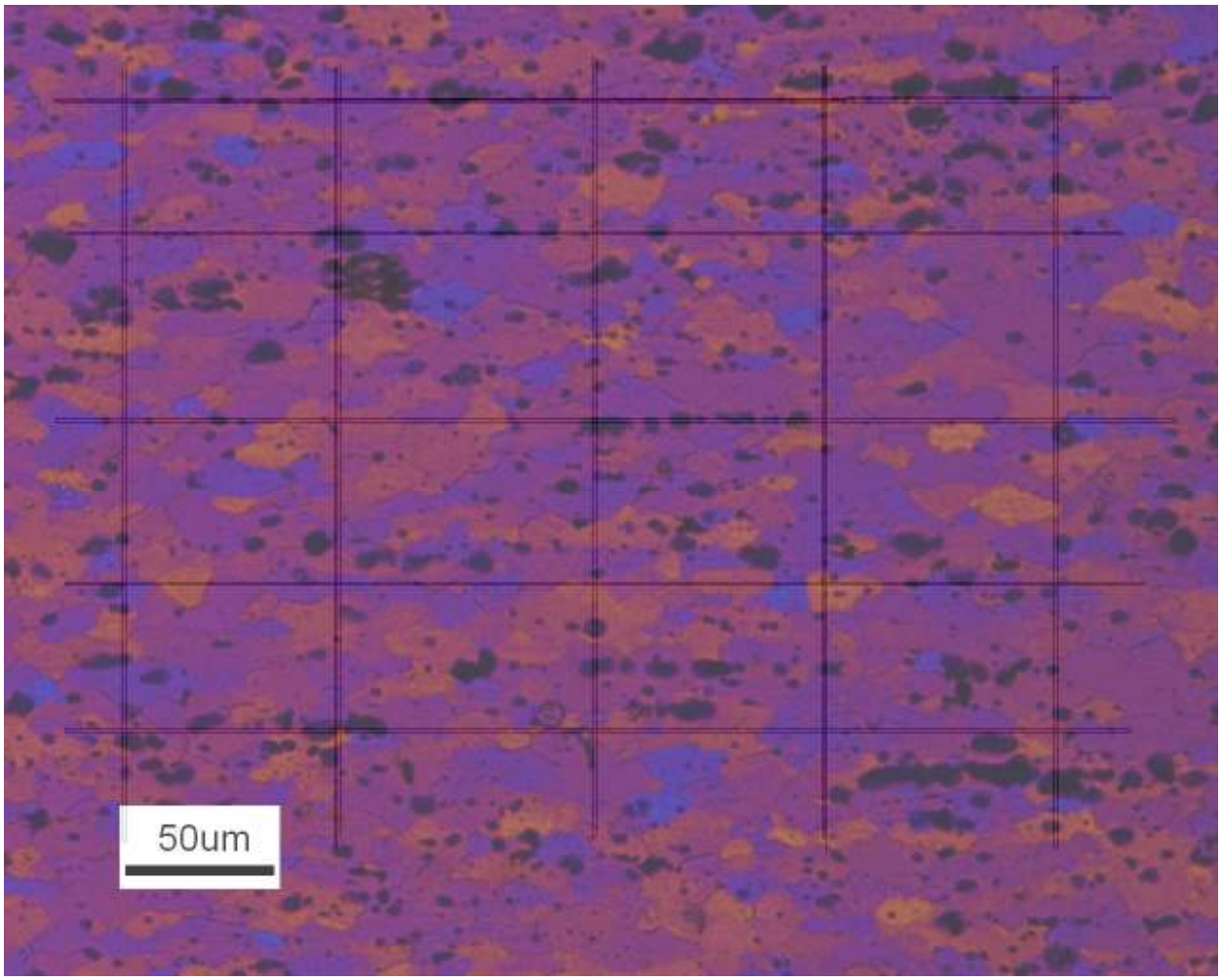

Fig 6-5 Photomicrograph of the cross section of the pole of bulge specimen tested at 400°C 2070 kPa; gridlines are shown over the microstructure for grain size measurements using the lineal intercept method, ASTM E112-10

Figure 6-5 shows a photomicrograph of the sample tested at 400°C and 2070 kPa (300 psi) after etching. This photomicrograph is representative of all the samples that were analyzed. The x direction in Figure 6-5 is the circumferential direction, and the y direction is through the thickness of the specimen. The polarizing filters give different colors to the grains, depending on their orientations, and help distinguish one grain from another. The gridlines included in the photo were used in the process of determining

average grain size. Grain sizes were determined by following ASTM E112, which governs the lineal intercept method of determining average grain size [36]. This method involves adding gridlines to a photomicrograph of a cross-section and counting the number of grains, or grain boundaries, across the distance of the gridline [36]. This was done multiple times both vertically and horizontally for each section of the two bulge specimens that were cross-sectioned. Chang measured the original grain size using the same ASTM method and determined that the average grain size was 14μm [9].

	Transverse Direction	Circumferential Direction
Test Section	Average Grain Size(μm)	Average Grain Size(μm)
400C 2070 kPa		
End	12.8	17.0
Middle	9.4	16.4
Pole	9.5	15.1
450C 2070 kPa		
End	11.5	14.7
Middle	11.2	19.7
Pole	11.5	18.8

Table 6-5 Average grain sizes of two samples taken at the pole, end and middle of the specimen after bulge testing.

Table 6-5 shows the results of the grain size measurements, and it shows that there was no abnormal grain growth in the specimens. The 450°C 2070 kPa sample shows that for the transverse direction, or through the thickness, the grains stayed roughly the same size from the end section to the middle and pole sections. However, the

circumferential direction shows an increase in average grain size indicating that there was some stretching of the grains involved. This stretching of the grains is consistent with the thickness direction becoming thinner while the circumferential direction becomes expanded. The 400°C 2070 kPa sample shows that the grain sizes get slightly smaller in the circumferential direction, but also that the grains in the transverse direction also get smaller, showing the compressing of grains through the thickness of the material. The difference in grain sizes between the pole sections of both specimens and the end sections of both specimens is small enough that it is concluded that there was no abnormal grain growth due to the biaxial bulge testing.

Chapter 7: Conclusions and Future Work

7.1 Conclusions

This investigation into the gas-pressure forming of aluminum alloy AA5182 shows that it is possible to accurately simulate the forming process, bulge dome height and bulge dome shape, of an AA5182 specimen at hot and nearly warm forming temperatures using the material constitutive model, Equation 7-1, which was developed in this study.

$$\dot{\varepsilon} = e^{-Q_c/RT} * 9 * 10^9 * (\mathrm{Sinh}(490.866 * \sigma/E)^{4.11}\ s^{-1} \qquad (7\text{-}1)$$

Bulge forming was accurately simulated using this material model, within defined uncertainty bounds, for all but four total cases where strain hardening was a significant contributor. Strain hardening proved to be a significant contributor at temperatures of 350°C and lower and pressures of 2070 kPa (300 psi) and higher. Strain hardening was not expected to occur based upon previous tensile studies. This strain-hardening must be taken into account when simulating gas-pressure bulge forming at these lower temperatures and higher pressures. A maximum experimental bulge dome height of 25mm was achieved in multiple experimental tests. This maximum experimental bulge dome height is roughly equal to the radius of the bulge dome for this test geometry, using sheet with a thickness of 1 mm. Changes in the microstructure and grain size of the material were also a concern during the experimental testing. Cross-sectional analysis of

two different experimental bulge domes at separate conditions revealed no abnormal grain growth within the material during the forming process.

7.2 Future Work

There are many future considerations for testing and areas of interest with warm forming of AA5182. The material constitutive model, shown in Equation 3-7, can be further tested at a variety of intermediate temperatures and pressures to help better characterize warm forming of AA5182. One of the additional questions found during this investigation relates to where the temperature induced softening of the material offsets the strain hardening of the material during forming. At a temperature of 350°C and a pressure of 2070 kPa there is significant strain hardening in the specimen during forming. However, at a temperature of 400°C and a pressure of 2070 kPa strain hardening of the material does not seem to be significant. A refined material model that accounts for strain-hardening will predict more accurately the conditions found within this study where strain-hardening was a significant factor in bulge forming.

Another step in the future work can be done by scaling the dimensions of the test specimen. This should include both the thickness of the sheet as well as the radius of the specimen to determine if there are any scaling effects that are not captured by the simulations. A specimen of twice the thickness at the current specimen diameter as well as a specimen of either half or double the current specimen diameter would be helpful in determining how the thickness of the material affects the maximum dome height. This will help determine the dome height limitations of the material in the experimental testing

and also indicate whether there are additional factors that need to be included in the current material model or if the current material model can be scaled up to other thicknesses or diameters without losing the accuracy that it currently holds.

Another future consideration would be to vary the shape of the dome that is being formed. A plane strain case would give a good indication of how well the material model works at predicting the bulge forming of a non-axisymmetric shape. This would require a new bulge test simulation file that is three dimensional. Multiple shapes could be tested to determine in which cases the material model does or does not work. This could be combined with previous recommendations of varying thicknesses to determine if there are any negative effects involved with changing the shape of the formed specimen as well as the thickness of the original material.

One of the last steps in determining the characteristics of gas-pressure forming of AA5182 would be to change to a closed die into which the specimen would form. This would result in information more pertaining to the interaction between the die and the material than the material itself. These factors would include temperature, forming pressure and the friction between the forming material and the die. There would also be localized thinning in the specimen in certain areas of the die, if the die is complex enough, which would affect the failure mechanism and could result in an early failure. These additional investigations would further characterize, and help determine the commercial viability of warm forming in AA5182.

References

1. Joachim Roesler, Harald Harders, Martin Baeker. *Mechanical Behaviour of Engineering Materials.* New York: Springer, 2007.

2. T.G. Nieh, J. Wadsworth, O.D. Sherby. *Superplasticity in Metals and Ceramics.* 40 West 20th Street, New York, NY, 10011: Cambridge University Press, 1997.

3. Eric M. Taleff, Ken Takata, Koji Ichitani. "Hot and Warm Deformation of AA5182 Sheet Materials: Ductility and Microstructure Evolution." *Proceedings of the 12th International Conference on Aluminum Alloys.* Yokohama, Japan, 2010.

4. Eric M. Taleff, Louis G. Hector, Jr, John R. Bradley, Ravi Verma, Paul E. Krajewski. "Local Thinning at a Die Entry Radius During Hot Gas-Pressure Forming of an AA5083 Sheet." *Journal of Manufacturing Science and Engineering Vol 132*, 2010: 011016-1 - 011016-7.

5. Louis G. Hector Jr., Paul E. Krajewski, Eric M. Taleff, Jon T. Carter. "High-Temperature Forming of a Vehicle Closure Component in Fine-Grained Aluminum Alloy AA5083: Finite Element Situations and Experiments." *Key Engineering Materials Vol. 433*, 2010: 197-210.

6. Nader Abedrabbo, Farhang Pourboghrat, John Carsley. "Forming of AA5182-O and AA5754-O at Elevated Temperatures Using Coupled Thermo-Mechanical Finite Element Models." *International Journal of Plasticity 23*, 2007: 841-875.

7. Daoming Li, Amit K. Ghosh. "Biaxial warm forming behavior of aluminum sheet alloys." *Journal of Materials Processing Technology 145*, 2004: 281-293.

8. O.D. Sherby, P.M. Burke. *Progress in Materials Science*, 1968: 325-390.

9. Jung-Kuei Chang, Ken Takata, Koji Ichitani, Eric M. Taleff. "Ductility of an Aluminum-4.4 wt. pct. Magnesium Alloy at Warm- and Hot-Working Temperatures." *Materials Science and Engineering A 527*, 2010: 3822-2828.

10. J. G. Schroth, Ed. By E. M. Taleff, P. A.Friedman, P. E. Krajewski, R. S. Mishra, and J. G. Schroth. "Advances in Superplasticity and Superplastic Forming." *TMS*, 2004: 9-20.

11. *ASM International Handbooks Online.* n.d. http://products.asminternational.org/hbk/index.jsp (accessed 11 10, 2011).

12. Anup Bandivadekar, Kristian Bodek, Lynette Cheah, Christopher Evans, Tiffany Groode, John Heywood, Emmanuel Kasseris, Matthew Kromer, Malcom Weiss. *On The Road in 2035: Reducing Transportation's Petroleum Consumption and GHG Emissions.* Massachusetts Institute of Technology, 2008.

13. G.S. Cole, A.M. Sherman. "Lightweight Materials for Automotive Applications." *Elsevier - Materials Characterization* (Ford Motor Company), 1995: 35:3-9.

14. Serkan Toros, Fahrettin Ozturk, Ilyas Kacar. "Review of Warm Forming of Aluminum-Magnesium Alloys." *Journal of Materials Processing Technology 207*, 2008: 1-12.

15. Hryn, B. Davis and J. *Innovative Forming and Fabrication Technologies: New Opportunities.* Final Report, Chicago: Argone National Laboratory, 2007.

16. American Society of Metals. *Metals Handbook Ninth Edition: Volumes 1 and 2.* 1978.

17. Lynette Cheah, John Heywood. "Meeting U.S. Passenger Vehicle Fuel Economy Standards in 2016 and Beyond." *Elsevier Energy Policy 39*, 2011: 454-466.

18. C. Molteni, Nicola Marzari, M. C. Payne, and V. Heine. "Sliding Mechanisms in Aluminum Grain Boundaries." *Physical Review Letters Vol 79 Number 5*, 1997: 869-872.

19. Taleff, Eric M. "An Overview of Hot and Warm Forming of Al-Mg Alloys." *Key Engineering Materials Vol. 433*, 2010: 259-265.

20. Gittus, J.H. "Theoretical Equation for Steady State Dislocation creep: Effect of Solute Drag." *Acta Metallurgica*, 1974: 1179-1181.

21. Ayres, Robert A. "Alloying Aluminum with Magnesium for Ductility at Warm Temperatures." *METALLURGICAL TRANSACTIONSA*, 1979: 849-854.

22. Mary-Anne Kulas, Eric M. Taleff, W. Paul Green, Paul E. Krajewski, Terry R. McNelley. "Deformation Mechanisms in Superplastic AA5083 Materials." *Metallurgical and Materials Transactions A*, 2005: 1249-1261.

23. Yeong-Maw Hwang, Jen-Shin Yang, Tsung-Rong Chen, Jacob B. Huang, Wun-Uven Wu. "Analysis of Superplastic Blow Forming in a Conical Die." *International Journal of Mechanical Science Vol 40*, 1998: 867-885.

24. 11 8, 2011. www.efunda.com.

25. W. Köster. *Zeitschrift für Metallkunde 39*, 1948: 1-9.

26. Eric M. Taleff, P. J. Nevland, and P. E. Krajewski. "Tensile ductility of several commercial aluminum alloys at elevated temperatures." *Metallurgical and Materials Transactions A*, 2001: 1119-1130.

27. Parviz Yavari, Farghalli A. Mohamed, Terence G. Langdon. "Creep and Substructure Formation in an Al-5%Mg Solid Solution Alloy." *Acta Metallurgica Vol 29*, 1981: 1495-1507.

28. E. Arzt, M.F. Ashby, R.A. Verrall. "Interface Controlled Diffusional Creep." *Acta Metallurgica Vol 31*, 1983: 1977-1989.

29. David L. Olmsted, Louis G. Hector Jr., W.A. Curtin. "Molecular dynamics study of solute strengthening in Al/Mg Alloys." *Journal of Mechanics and Physics of Solids 54*, 2006: 1763-1788.

30. Vanegas, Ricardo. *Design and Fabrication of an Instrument to Test the Mechanical Behavior of Aluminum Alloy Sheets During High-Temperature Gas-Pressure Blow-Forming.* Master's Thesis, Austin: University of Texas at Austin, 2008.

31. "AbaqusTM." www.simulia.com

32. Carpenter, Alexander. *The Effects of Processing Conditions on Static Abnormal Grain Growth in Al-Mg Alloy AA5182.* Master's Thesis, Austin: University of Texas at Austin, 2011.

33. Sherek, Paul. *Simulation and Experimental Investigation of Hot Gas-Pressure Forming for Light-Alloy Sheet Material.* Master's Thesis, Austin: University of Texas at Austin, 2009.

34. Mary-Anne Kulas, W. Paul Green, Eric M. Taleff, Paul E. Krajewski, Terry R. McNelley. "Failure Mechanisms in Superplastic AA5083 Materials." *Metallurgical and Materials Transactions*, 2006: 645-655.

35. Chang, Jung-Kuei. *The Effect of Microstructure on Cavitation during Hot Deformation in Fine-grained AA5083 Aluminum Alloy Sheet Material.* PhD Dissertation, Austin: University of Texas at Austin, 2008.

36. International, ASTM. "Standard Test Methods for Determining Average Grain Size." By ASTM International. West Conshohocken, 1996.